THE HONG KONG
POLYTECHNIC UNIVERSITY
香港理工大學
Pao Yue-kong Library
包玉剛圖書館

Copyright Undertaking

This thesis is protected by copyright, with all rights reserved.

By reading and using the thesis, the reader understands and agrees to the following terms:

1. The reader will abide by the rules and legal ordinances governing copyright regarding the use of the thesis.

2. The reader will use the thesis for the purpose of research or private study only and not for distribution or further reproduction or any other purpose.

3. The reader agrees to indemnify and hold the University harmless from and against any loss, damage, cost, liability or expenses arising from copyright infringement or unauthorized usage.

DIRECTLY PRINTED PLASMONIC SENSORS OF GOLD MICRO/NANO-STRUCTURES FOR BIOCHEMICAL DETECTION

WU HAO

MPhil

The Hong Kong Polytechnic University

2023

The Hong Kong Polytechnic University

Department of Electrical Engineering

Directly Printed Plasmonic Sensors of Gold Micro/Nano-Structures for Biochemical Detection

WU Hao

A thesis submitted in partial fulfilment of the requirements for the degree of Master of Philosophy

December 2022

CERTIFICATE OF ORIGINALITY

I hereby declare that this thesis is my own work and that, to the best of my knowledge and belief, it reproduces no material previously published or written, nor material that has been accepted for the award of any other degree or diploma, except where due acknowledgement has been made in the text.

_____(Signed)

_____WU Hao_____(Name of student)

Abstract

Plasmonics is an emerging technology that has many important applications, such as biochemical detection. Especially in recent years, with the development of micro/nano fabrication technology and numerical simulation tools, research on the mechanism and application of localized surface plasmon resonance (LSPR) has attracted more attention. One of the most important optical effects of LSPR is the localization of the electromagnetic field at certain regions of the nanostructure's surface (or, in other words, the local field is "enhanced"). The tight confinement of local electromagnetic fields by metallic nanostructures can lead to many novel optical effects and provide opportunities for light-matter interactions at the nanometer-scale level. Such a unique property can be harnessed to develop high-performance optical biosensing technologies, such as LSPR label-free biosensing and plasmonic substrates for plasmonically-enhanced IRAS biodetection. In this thesis, we develop two kinds of directly printed plasmonic biosensors for LSPR label-free biosensing and plasmonically-enhanced IRAS biochemical detection, respectively.

Firstly, an optical fiber-tip biosensor based on micropatterns of gold nanoparticles is developed. The flat end-face of optical fiber makes it a uniquely ultrasmall substrate which provides opportunities for the development of many ultrasmall optical sensors and devices. Its small size allows the access to space-restricted environments, while its good biocompatibility, chemical resistance, and mechanical robustness make it very suitable for biosensing applications. After printing of plasmonic structures upon optical

fiber end-face, a highly compact and sensitive biosensor can be fabricated. We developed an *in-situ* precision photoreduction technology to directly print plasmonic nanoparticles on the fiber end-face and thereby fabricate optical fiber-tip plasmonic biosensors. The fabricated sensors have been successfully demonstrated to detect the antibody and SARS-CoV-2 mimetic DNA sequence at the concentration levels of less than 100 ng/mL and 0.8 pM, respectively.

Secondly, a plasmonic substrate of periodic gold micro-flake array is developed for plasmonically-enhanced infrared absorption-spectroscopy biodetection. Plasmonic gold micro-flakes are directly printed by using precision photoreduction technology. Their spectral peaks of plasmonic resonances are tuned by the geometric parameters of the structure to match with the absorption peak of target molecules in the infrared region. The spectral responses of such plasmonic substrates are measured and compared with numerical results simulated by using COMSOL. A plasmonically enhanced infrared absorption-spectroscopy has been demonstrated by using the fabricated plasmonic substrate to detect BSA at the concentration level of 10 nM.

Publications arising from the thesis

Journal papers:

1. Y. Zhang[†], **H. Wu**[†], H. Wang, B. Yin, S. H. D. Wong, A. P. Zhang, and H. Y. Tam, "Ultraminiature optical fiber-tip directly-printed plasmonic biosensors for label-free biodetection." *Biosensors and Bioelectronics*, Vol. 218, p. 114774, 2022. (IF: 12.54; [†] Equally contributed to the work).

2. **H. Wu**, Y. Zhang, and A. P. Zhang, "Directly printed plasmonic substrate of periodic gold micro-flake array for infrared absorption-spectroscopic biodetection", in preparation.

Conference paper:

1. Y. Zhang, **H. Wu**, and A. Ping Zhang. "A thin-film optical filter with in-cavity strongly-coupled silver nanoparticles." *Optoelectronics and Communications Conference* (OECC 2021), Hong Kong, July 3 – 7, 2021.

Acknowledgements

This MPhil dissertation can't be completed without the help from many people. Their support will always be remembered by me.

First and foremost, I want to say that I am sincerely thankful to my supervisor Prof. A. Ping Zhang for his great support not only in my research but also in my life here. For this thesis, from the topic selection to the completion, every step is completed under the careful guidance of Prof. A. Ping Zhang. His rigorous academic spirit, profound knowledgement and tireless pioneering spirit have deeply infected me, which will be unforgettable throughout my future life.

I also would like to thank Dr. Yangxi Zhang who offered a lot of help with experiment designs, sensor fabrications and characterizations. He is a thinker and always gives us innovative ideas. I am impressed by his passion and enthusiasm for research which will influence me in the future. I would like to thank Dr. Venkata Krishnaiah who helped me with the sensor preparation. I am very grateful to Dr. Xin Cheng and Dr. Jitendra Narayan Dash for their support in the setup of optical fiber cleaver and fusion splicer. Besides, I appreciate Dr. Jinhui Wang, Dr. Jingxian Cui, Miss. Han Wang, Mr. Taige Li, Mr. Zhizheng Wang, Mr. Chun Yip Ho, Mr. Yiang Qin for their help and useful discussions on my experiments. Moreover, I am much appreciated for my friends in Hong Kong who care about me and always encourage me.

Lastly, it is my family's love and support that has helped me go this far and this thesis

is dedicated to them. Without them, it is impossible to complete this thesis.

Table of Contents

List of Figures

List of Acronyms

Acronyms	Description
ADDL	Amyloid-β-derived diffusible ligand
BSA	Bovine serum albumin
CSF	Cerebrospinal fluid
DI	Deionized
DLW	Direct laser writing
DMD	Digital-micromirror device
EBL	Electron beam lithography
FEM	Finite element method
FIB	Focused Ion Beam
FO	Fiber optic
FOM	Figure of merit
FTIR	Fourier-transform infrared spectroscopy
GMRA	Gold mushroom array
IgG	Immunoglobulin G
IPA	Isopropyl alcohol
IR	Infrared
IRAS	Infrared absorption spectroscopy
LOD	Limit of detection

LSPR	Localized surface plasmon resonance
MEF	Metal-enhanced fluorescence
NIL	Nanoimprint Lithography
NP	Nanoparticle
PBS	Phosphate buffered saline
PPL	Projection Photolithography
PRET	Plasmon resonance energy transfer
PSPR	Propogation surface plasmon resonance
RI	Refractive index
RIU	Refractive index unit
SEIRAS	Surface-enhanced infrared absorption spectroscopy
SEM	Scanning electron microscope
SERS	Surface-enhanced Raman spectroscopy
SP	Surface plasmon
SPP	Surface plasmon polariton
SPR	Surface plasmon resonance
UV	Ultraviolet

Chapter 1

Introduction

1. 1 Research background

Surface plasmon resonance (SPR) is a well-known phenomenon widely existing in various metallic materials. Plasmonic substrates which are normally made of gold or silver nanostructures based on this phenomenon can provide benefits to many scientific disciplines. As can be seen from **Fig. 1.1**, when the size of gold/silver nanostructures is a few to around 100 nm, a collective oscillation of free electrons may occur in the metallic nanostructures, called localized surface plasmon resonance (LSPR).
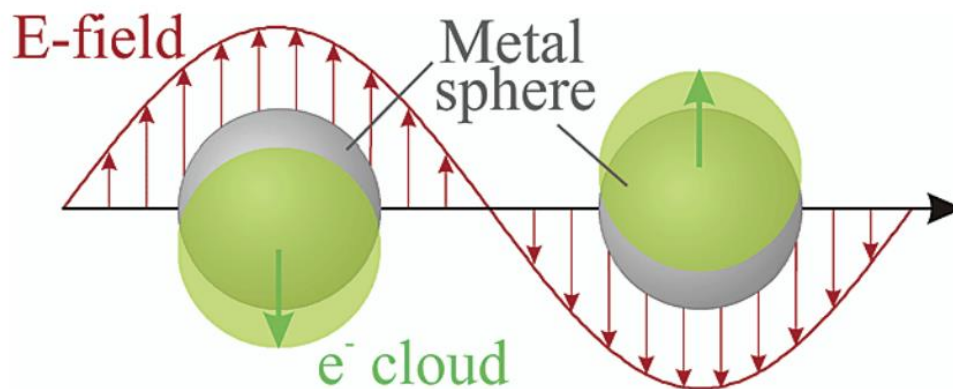
Figure 1.1 Localize surface plasmons. Adapted from Ref[1].

It is important to note the unique optical property of LSPR that it can greatly enhance the electric field around the nanoparticle's surface. Such an ability of high confinement and enhancement of electric field can be utilized to enhance the signal in biosensing

applications, in which normally a tiny amount of target analyte is used for spectroscopic biodetection and its signal is typically very weak. Therefore, nowadays many applications including surface-enhanced Raman spectroscopy (SERS) [2], plasmon-enhanced fluorescence [3], and surface-enhanced infrared absorption spectroscopy (SEIRAS) [4] have adopted LSPR excitations as a method to enhance light-matter interactions.

1.1.1 The physics of plasmons

Proposed by David Pines in the 1950s, the concept 'plasmon' was first used to describe energy loss in the metal which was caused by free electrons' collective oscillation [5]. These plasmon oscillations are regarded as free electron's mechanical oscillations caused by the external electromagnetic field (incident light). For plasmons at the surface of metal materials, they are called surface plasmons (SPs) or surface plasmon resonance (SPR) [5].

Usually, plasmons are excited by coupling mechanisms with electromagnetic waves. There are three main groups of plasmons. First, bulk plasmons correspond to collective longitudinal electron oscillations at plasmonic frequencies. Second, the so-called PSPR is that the surface plasmon excited at the interface between metal nanofilm and dielectric medium can propagate a long distance along them [6]. And finally, the free electron oscillation in metal nanoparticles limited by the plasmonic structure's geometries is called localized SPR [7-8].

In propagation SPR, surface plasmons are generated by electron oscillations by an electromagnetic field [9]. They can only exist at the interface between positive and negative constant media. The medium with a positive permittivity (often called a dielectric) can be any transparent material, such as air or glass. Negative dielectric constant media, commonly referred to as plasmonic media, can be metals or other materials [10]. Among natural materials, only metals and some doped semiconductors have plasmonic properties due to high plasmonic frequencies caused by abundant free electrons. Derived from Maxwell's equations, the relationship between the propagation constant of the SPs and that of incident light is obtained as follows:

$$k_{sp} = k_0 \left(\frac{\varepsilon_d \varepsilon_m}{\varepsilon_d + \varepsilon_m} \right)^{\frac{1}{2}} \qquad (1.1)$$

where k_{sp} and k_0 denote the wave vector of the SPs and the incident light at wavelength λ, respectively; ε_m and ε_d denote the wavelength-dependent dielectric constants of the metal and dielectric, respectively.

From equation (1.1), the momentum of the incident light and the SPs differ from each other. Therefore, in order to correct this mismatch different coupling methods are introduced for the excitation of SPR, including prism coupling [11], grating coupling [12], fiber coupling [13] and so on. Sensors based on SPR have found applications in many fields and compared with other sensing techniques they are known for their high sensitivity, simplicity of operation, and quick and easy detection.

In terms of LSPR, the mechanism behind it is quite different from that of propagation SPR. This effect appears due to the nontrivial scattering properties of subwavelength-sized conducting objects in oscillating electromagnetic fields. In LSPR, a nanoparticle

19

of which the size is smaller than the incident light's wavelength can generate the localized surface plasmon, and if the nanoparticle is under resonance conditions, which are influenced by the geometry, composition and surrounding environment of the nanoparticle, its free electrons can oscillate together. This will lead to the enhanced electric fields near the nanoparticle's surface where a maximum electric field is achieved and it will rapidly fall off with distance. To fully understand this phenomenon, Mie theory is used to demonstrate how LSPR occurs. The Mie solution for the nanoparticles plasmon resonance is shown as follows

$$\sigma_{ext} = \frac{18\pi\varepsilon_d^{3/2}V}{\lambda} \frac{\varepsilon_2(\lambda)}{\left[\varepsilon_1(\lambda) + 2\varepsilon_d\right]^2 + \varepsilon_2(\lambda)^2} \tag{1.2}$$

where σ_{ext} is the extinction cross-section, V is the volume of the nanoparticle, λ is the wavelength of the incident light, ε_d and $\varepsilon_m(\lambda) = \varepsilon_1(\lambda) + i\varepsilon_2(\lambda)$ are the dielectric function of the surrounding medium and the metal, respectively. It is found that equation (1.2) is maximized when $\varepsilon_1(\lambda) = -2\varepsilon_d$. This indicates a resonance condition for the appearance of LSPR.

Although the resonance condition is deduced from equation (1.2), it still does not directly show the influence of the surrounding medium's refractive index on the LSPR peak wavelength. The ε_1 could be further expanded using the Drude model of metals and it is described as:

$$\varepsilon_1 = 1 - \frac{\omega_p^2}{\omega^2} \tag{1.3}$$

where ω_p is the plasmon frequency and ω is the angular frequency of the incident light. When the resonance condition is met, by applying the medium's dielectric

function $\varepsilon_d = n_d^2$ the LSPR peak wavelength is obtained:

$$\lambda_{\max} = \lambda_p \sqrt{2n_d^2 + 1} \tag{1.4}$$

where $\lambda_{\max}$ is the LSPR peak wavelength, λ_p is the wavelength corresponding to the plasmon frequency of the bulk metal and n_d is the refractive index of the surrounding medium. Therefore, it reveals that the LSPR peak wavelength changes linearly according to the refractive index. This almost linear relationship is the basis of many LSPR sensing applications.

1.1.2 LSPR biosensors

The first realization of the plasmonic effect in sensing applications can be traced back to the early 1980s [14-16]. It started with the first pioneering work by Liedberg et al. who proposed the use of Kretschmann-Raether prism geometry to track recognition/binding events on planar Au surfaces [15]. This setup benefits from the SPP's dependence on environmental conditions and the fact that the RI of saline is different from most biological species' RI. And then, a commercial unit was built based on this proposed sensor [16]. The excellent performance of this sensing technology and the profound demand for biological detection subsequently led to many other SPR- and LSPR-based sensors.

Localized surface plasmon resonance, considered an extension of SPR, is achieved by using metallic nanostructures [17, 18]. When metals are separated into subwavelength nanoparticles, the high reflectivity of smooth noble metal films changes

dramatically which leads to plasmonic resonances. The LSPR peak wavelength can be tuned by optimizing the geometries of the nanostructure. Normally, the LSPR biosensors can be used for refractive index sensing and molecular sensing as shown in **Fig. 1.2**.
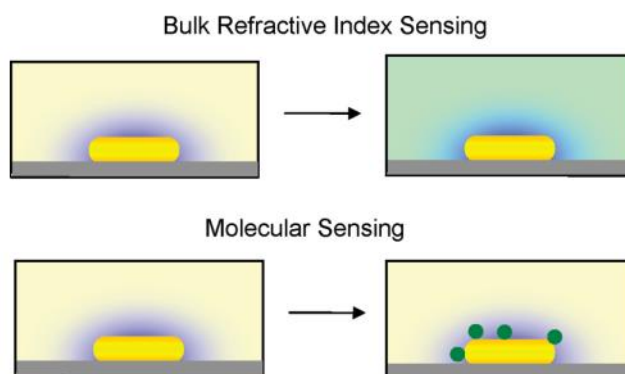
Figure 1.2 Comparison of bulk refractive index sensing and molecular sensing using LSPR. Adapted from Ref [8].

The former one is the simplest application in this aspect which is to monitor the movement in LSPR spectrum so as to detect the refractive index change in the environment. **Figure 1.3 (D, E)** show two kinds of gold nanoparticles which are nanorods and nanobipyramids, respectively, for refractive index sensing. Their extinction spectra are obtained by varying the solution's refractive index, see **Figure 1.3 (A, B)**. As the refractive index increases, both of their LSPR peaks shift to longer wavelengths. However, since these two structures differ, the strength of their response is not the same. Besides, **Figure 1.3 (C)** shows an approximately linear relationship between the LSPR peaks and the refractive index from 1.33 to 1.47 for these two kinds of gold nanoparticles.
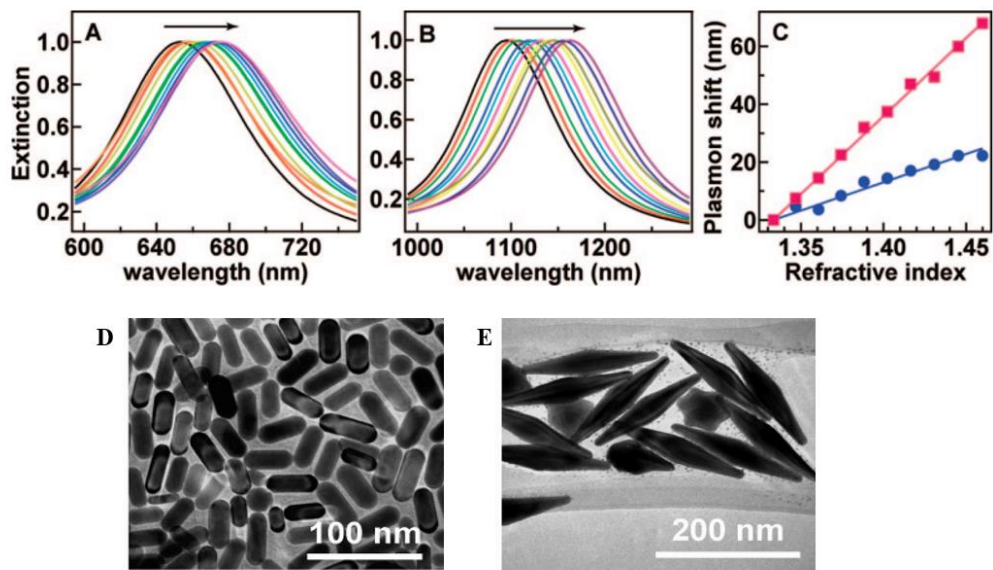
Figure 1.3 (A) Au nanorod's and (B) Au nanobipyramid's extinction spectra. The arrows indicate the direction of increasing refractive index. Au nanorod's (blue circles) and nanobipyramid's (red squares) responses to the refractive index change are ploted in (C).The TEM images of Au nanoparticles used for refractive index sensing in (A) and (B) are as shown in (D) Nanorods and (E) Nanobipyramids. Adapted from Ref [19].

In LSPR sensing, the achievable accuracy with respect to refractive index changes depends on sensitivity and peak linewidth. Larger nanoparticles can provide a higher sensitivity, but their peaks are broadened by multipolar excitation and radiative damping. Therefore, to characterize the detection capability of nanoparticles, a figure of merit (FOM) which is the sensitivity divided by the resonance linewidth is widely used [20]. Typically, the LSPR sensors' FOM values are normally smaller than the sensors based on the propagating SPR, preventing the widespread adoption of them.

To further improve the performance of LSPR sensors, Yang Shen et al. proposed a refractive index sensor with a figure of merit of refractive index sensing close to the theoretical limit [21]. A plasmonic gold mushroom array (GMRA) with top- and side-view shown in **Fig 1.4 (d, e)** was fabricated by double two-beam interference

lithography. The performance of GMRA was evaluated by immersing it into solutions with different refractive indices while monitoring its spectrum presented in **Fig. 1.4 (a, b)**. Its spectrum red-shifted with the increase of refractive index and a high refractive index sensitivity of 1,015 nm RIU was obtained from linear fitting, see **Fig. 1.4 (c)**. Notably, GMRA has determined FOM values between 80 and 108, which are significantly higher than the values of other LSPR-related sensors and even comparable to the upper theoretical estimate (~108) of a standard PSPR sensor [22, 23].
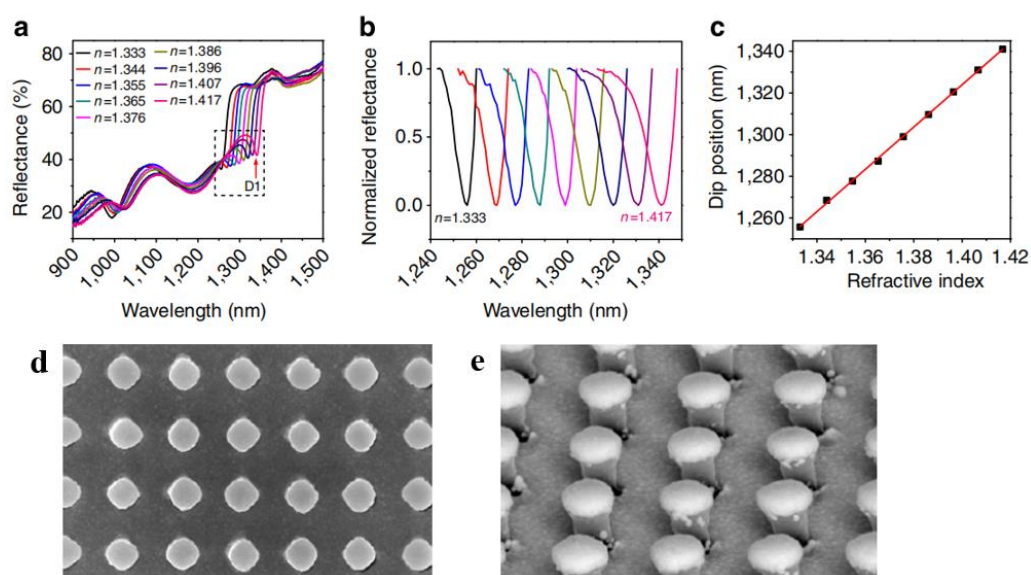
Figure 1. 4 (a) Reflectance spectra of the plasmonic structure. (b) Normalized reflectance spectra for D1 region in (a). (c) Relationship between the wavelength of D1 (solid squares) and the refractive index. (d, e) SEM images of the plasmonic structures from top and side, respectively. Adapted from Ref [21].

In terms of molecular sensing, we can consider it as an expansion from sensing the local environment to detecting biomaterials. Since the electric field enhancement of LSPR will rapidly fall off from the nanoparticle's surface, it means the sensing region is in the nanoscale around the nanoparticle. Therefore, such a highly localized sensing area is especially suitable for monitoring the molecular interaction existing around the

nanoparticle's surface. The very first reported works based on this principle detected streptavidin by monitoring the LSPR peak wavelength [17, 24]. Experiments measuring concanavalin A binding to mannose-functionalized nanoparticles followed these initial experiments [25]. After exposure to concanavalin A, the LSPR peak wavelength of these nanoparticles of different thicknesses was monitored with time. After a certain time, the sensor was washed with buffer resulting in the decrease of LSPR peak wavelength shifts, see **Figure 1.5**. Moreover, in all cases, the LSPR peak wavelengths share similar time constants of response to the analyte, but their overall shift magnitudes differ. In terms of the thinnest nanoparticles, they possess the largest LSPR wavelength shift response, which is consistent with distance-dependent experiments. These experiments have revealed the significance of the aforementioned fundamental spectroscopy studies. Moreover, they give guidance on the design of the following LSPR research.
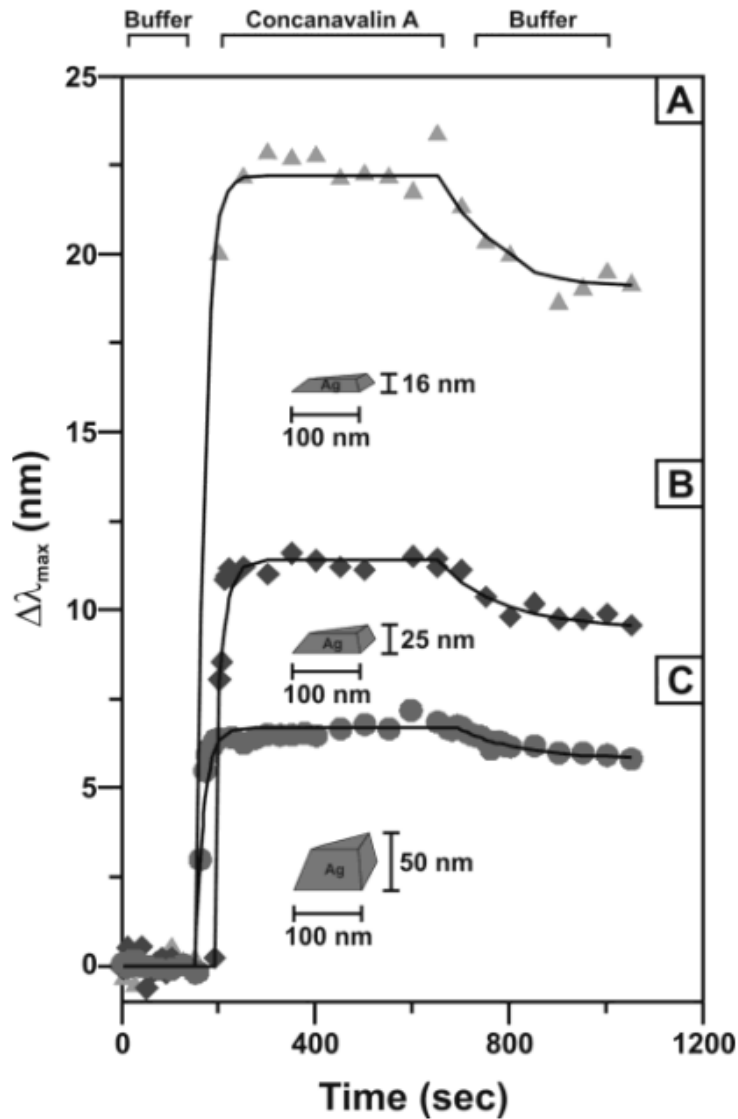
Figure 1. 5 Real-time response of Ag nanosensor interacted with concanavalin A. Adapted from Ref [25].

Detection of the Alzheimer's disease biomarker amyloid-β-derived diffusible ligand (ADDL) is one of the most biomedically relevant demonstrations of LSPR sensing [26-28]. In their experiments, the researchers developed a sandwich-like detection process as shown in **Figure 1.6 (A)**. A nanoparticle array is fabricated and the antibody for the detection of ADDL molecules is attached to them. After the interaction between the antibody and ADDL molecules, another capping antibody is used, which can bind to surface-bound ADDL to complete the sandwich assay. As low as 100 fM ADDL that

could be detected was achieved by these experiments. Based on that, other experiments were performed using cerebrospinal fluid (CSF) from the age-matched controls and target patients, respectively [29].
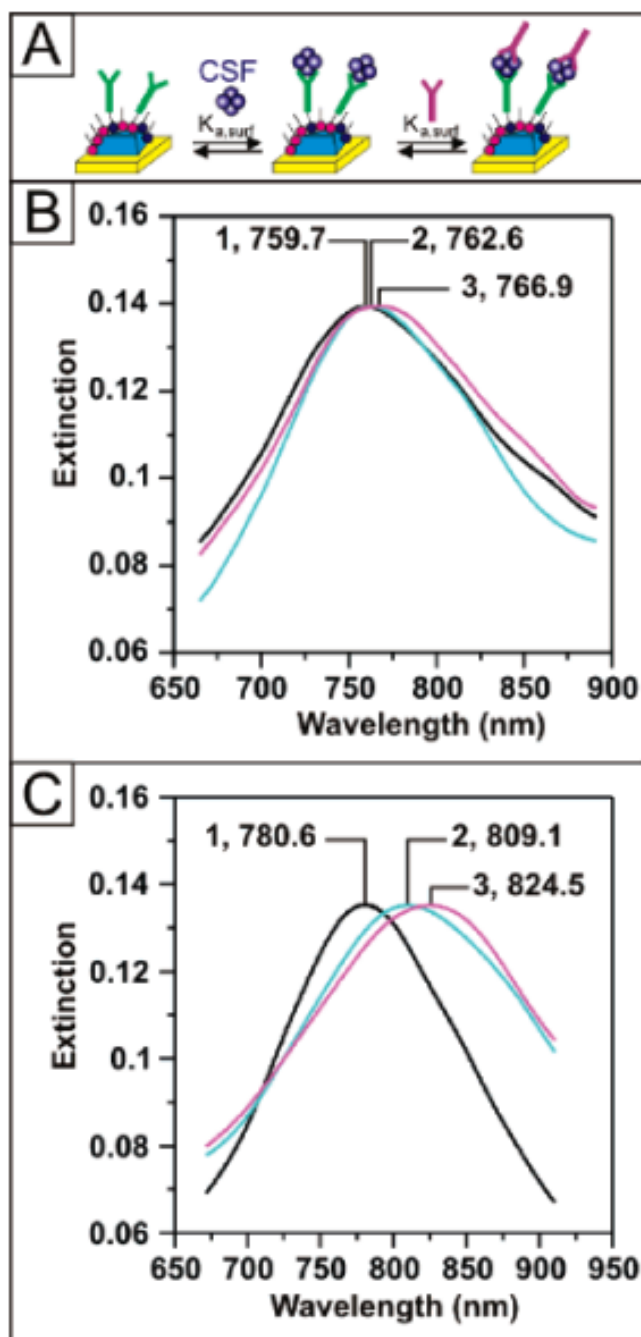
Figure 1. 6 Analysis of human CSF samples using a LSPR nanosensor. (A) working principle of this LSPR nanosensor. LSPR spectral of this nanosensor for the analysis of human CSF taken from (B) age-matched control patients and (C) patients with Alzheimer's disease. Adapted from Ref [29].

In **Figure 1.6 (B)**, CSF from age-matched control patients was exposed to anti-ADDL functionalized nanoparticles. The changes in LSPR spectra were modest (2.9 and 4.3 nm, respectively) during interaction of either CSF or the second capping antibody, which was mainly due to the refractive index change since there were no specific bindings. However, for a patient, the data was quite different as shown in **Figure 1.6 (C)**. Here, the binding of ADDLs in the CSF caused a shift of 28.5 nm and a further shift of 15.4 nm after the introduction of the secondary antibody. Similar results were found when using brain extracts rather than cerebrospinal fluid. Therefore, based on these experimental results it is clear that LSPR spectroscopy is a powerful technique to detect this Alzheimer's disease biomarker. Furthermore, this approach can be broadly popularized to diagnose any disease using relevant biomarker-antibody bindings such as ovarian cancer.

1.1.3 Plasmonically-enhanced infrared absorption spectroscopy for biochemical detection

Infrared spectroscopy is a widely adopted method with a strong ability for the identification of molecular species based on their vibrational modes in IR range. Because of its capability to provide a "fingerprint" of the target molecule as shown in **Figure 1.7**, this technique is of significant importance in research and industry.
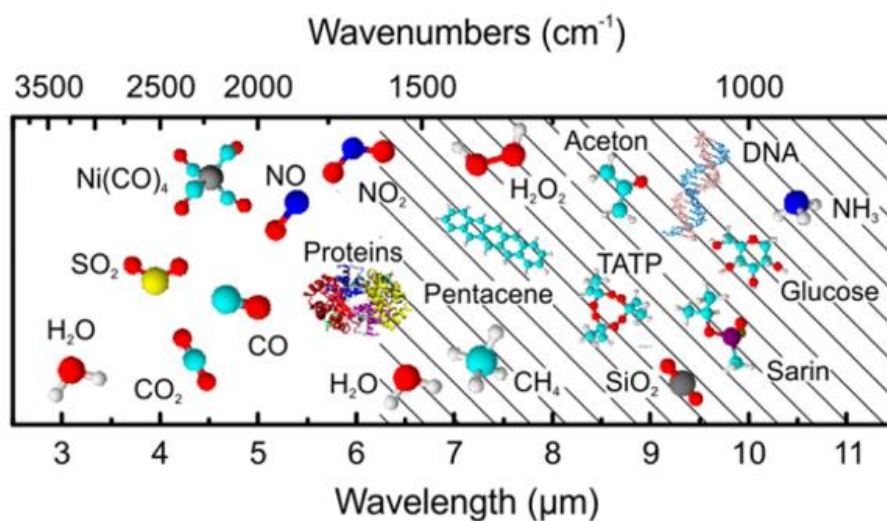
Figure 1.7 Characteristic infrared vibrations of selected molecular species. The fingerprint region containing skeletal vibrations is hatched. Adapted from Ref [30].

However, limited by the low absorption cross-sections, using minute amounts of materials for the Infrared-spectroscopy analysis tends out to be difficult and challenging. To overcome this problem, several methods have been proposed. Among them, optimizing the IR light source or improving the IR detector's sensitivity is quite an efficient way to solve this problem but the cost is large. Compared to them, plasmonically-enhanced infrared absorption spectroscopy is cost-effective and it has the ability to greatly enhance the detection sensitivity up to several orders of magnitude via the localized electric field at the metallic structure's surface based on LSPR [31-33]. Experimental results for this technique were first presented in 1980 by Hartstein et al. [34]. A thin film deposited with randomly arranged silver nanoparticles was used for their demonstrations. With a 60 Å film as shown in **Fig. 1. 8,** an enhancement factor of 20 was obtained which was not high enough due to the mismatch between the plasmonic resonance of these randomly arranged silver nanoparticles and the IR

absorption peak of the analyte.
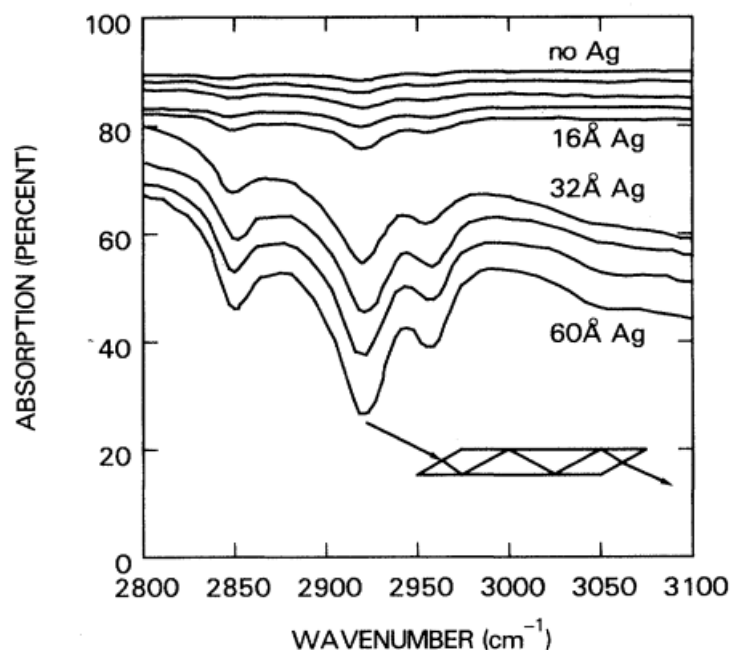
Figure 1.8 Absorption of the C-H modes of a monolayer of 4-nitrobenzoic acid using different thickness of Ag film. The curves have been offset for clarity. Adapted from Ref. [34].

Since these silver nanoparticles' plasmonic resonance was located at the visible range, a stronger enhancement could be obtained if the LSPR is tuned to the target infrared absorption region and even a maximum enhancement is achievable when the plasmonic resonance matches with the vibrational mode of the analyte. This maximum enhancement is quite desirable for plasmonically-enhanced IRAS sensing. Therefore, in 2008, Neubrech et al. first proposed using a resonant gold nanoantenna for plasmonically-enhanced IRAS [33]. In their experiment, different lengths of single gold nanoantennas were fabricated by electrochemical deposition followed by a transfer process. To monitor their plasmonically-enhanced IRAS activity, a model analyte formed of octadecanethiol (ODT) deposited on the gold nanoantennas' surfaces was

used. The incident light is polarized parallel to the long axis of the gold nanoantennas.

As seen in **Fig 1. 9**, fundamental plasmonic excitations of the gold nanoantennas

appeared around 3000 cm^{-1} indicated by the extinction spectra. Moreover, within the

broadband plasmonic resonances, there were several narrowband spectral signatures

resulting from the IR absorptions of ODT.
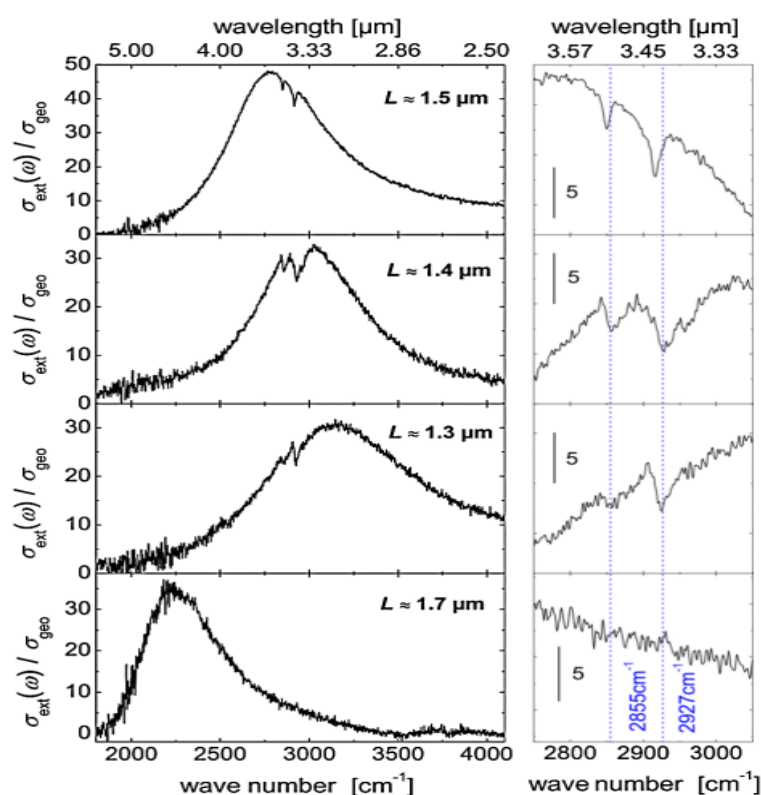
Figure 1.9 Extinction spectra of four ODT-coated gold nanoantennas with different length on CaF$_2$. Right side: the zoom to the vibrational signals. Dotted lines: ODT vibration frequencies. Adapted from Ref. [33].

In addition, these gold nanoantennas' plasmonic resonances were tuned by changing

their lengths. And thus, the plasmonically-enhanced IRAS activity was influenced by

the relationship between plasmonic resonance and vibrational frequency. If the

plasmonic resonance matches with the ODT's vibrational modes, the strongest

plasmonically-enhanced IRAS enhancement could be realized. On the contrary, the 1.7

μm long gold nanoantenna demonstrated a detuned plasmonic resonance from vibrational frequency resulting in no vibrational signals. It reveals the plasmonically-enhanced IRAS sensing's resonant nature.

Moreover, with the development of nanofabrication technologies including electron beam lithography (EBL) [35], direct laser writing (DLW) [36], UV-lithography [37] and so on, many well-defined metallic nanostructures have been demonstrated andexhibit relatively larger IR plasmonic enhancement. For example, in 2009, Adato et al. first demonstrated the usage of collective excitations from plasmonic nanoantenna arrays [35]. The fabricated periodic arrays of rod-shaped antennas are as shown in **Fig. 1.10 (A)**. After coating with protein, in their reflection spectra, their absorption bands are clearly noticeable as can be seen in **Fig. 1.10 (B)** located at 1,660 and 1,537 cm^{-1}. **Fig. 1.10 (C)** shows the difference spectra of the periodic and the randomized arrays. The periods of these nanoantennas arrays were from 1.5 to 2.0 μm which tuned their plasmonic resonances. Therefore, different absorption intensities of the protein layer were obtained.
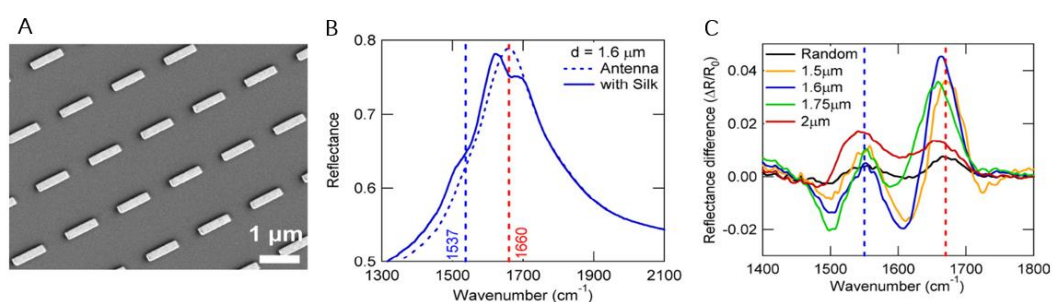
Figure 1.10 (A) Scanning electron microscope (SEM) images of a periodic array of gold nanoantennas. (B) Reflectance spectra from the 1.6 μm periodic array before (dashed line) and after coating of 2 nm thick protein film (solid line). (C) Difference absorption spectra of the periodic and randomized arrays. Adapted from Ref. [35].

With the surface lattice resonances of large-area mid-infrared antenna array, a significant narrowing of the resonant spectral peak whose quality factor exceeds 200, was reported by Bar Cohn et al. in 2021 [38]. Large-area (4 × 4 mm) arrays of infrared antennas were prepared on CaF_2 substrates using EBL as can be seen in **Fig. 1.11 (A)**. The surface lattcie resonance appears when the resonance of the individual nanoantenna is slightly shorter than the wavelength of the diffraction order of the nanoantenna array. Control over the resonance wavelength can be achieved by modifing the length of infrared antennas and tuning the strength of the interactions among nanoantennas through changing the period. An extremely narrow resonance is presented in **Fig. 1.11 (B)**. A quality factor of around 200 is obtained and a strong coupling can be achieved by tuning this resonant peak to match with molecular absorption bands.
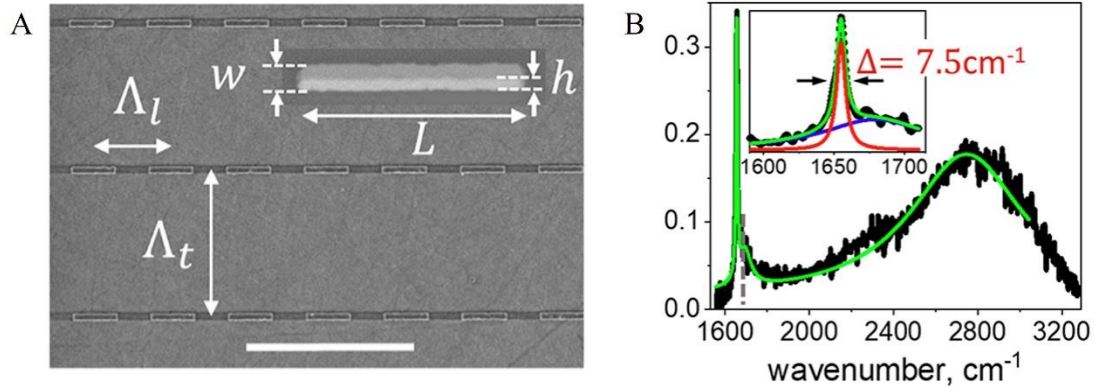
Figure 1.11 (A) Scanning electron microscope (SEM) images of periodic arrays of infrared antennas. (B) Normal-incidence spectra of an infrared antenna array. The inset illustrates the ALP peak in greater detail. The narrowband resonance component corresponds to $Q = 220$. Adapted from Ref. [38].

There are many other works using the nanofabricated plasmonic nanoantennas and this kind of structure possesses of many advantages like significantly huge enhancement to the signal and precise control over plasmonic resonance [39-41].

1. 2 Motivations and objectives of research

Plasmonic metallic substrates for different applications have been intensively studied for decades and various fabrication technologies have been proposed for the preparation of these devices. However, there is no perfect fabrication technique. For example, electron-beam lithography's resolution is sufficient for precisely fabricating metallic substrates of well-defined nanostructures [42]. However, the need to use expensive equipment and its own working manners make it costly and have a low-throughput problem. Other techniques, like deposition methods including sputtering [43], evaporation [44], and electrodepositon [45] can achieve rapid preparation for metallic substrates. But these techniques cannot direct fabricate designed structures on micro/nano scale and the need for further lithography makes the fabrication more complicated. Therefore, developing a simple, rapid, inexpensive yet durable fabrication process for metallic substrates still remains a challenge. The objective of this research is to fabricate plasmonic metallic sensors using previously developed precision photoreduction technology and explore their applications on LSPR sensing and plasmonically-enhanced IRAS biosensing. In this thesis, two kinds of plasmonic metallic sensors are developed. For the first one, the AuNPs are printed on the end surface of the multimode fiber and the appilcations for the detection of antibody and DNA sequence are demenstrated. For the second one, plasmonic substrates formed by periodic gold micro-flake array are fabricated and they can be applied to plasmonically-enhanced IRAS biodetection of BSA.

1. 3 Outline of thesis

The chapters of this thesis are organized as below:

Chapter 1: Introduction. In this chapter, the background of the topics involved in this work is presented including the physics of surface plasmons, LSPR sensing basics and plasmonically-enhanced infrared absorption spectroscopy. The motivations, objectives of this work are given, and the outline of this thesis is also described.

Chapter 2: Precision photoreduction technology. In this chapter, different micro/nano fabrications technology are presented. Their advantages and drawbacks are described. Next, the precision photoreduction technology for selectively printing of AuNPs is presented in detail.

Chapter 3: Optical fiber-tip directly-printed plasmonic biosensor for label-free biodetection. In this chapter, the AuNPs are directly printed on the multimode fiber-tip using the precision photoreduction technology. The fabricated sensors have been used for the detection of target antibody and DNA sequence. The performance of this sensor is presented in detail.

Chapter 4: Directly printed plasmonic substrate of periodic gold micro-flake array for IRAS biochemical detection. In this chapter, the plasmonic substrates of gold micro-flake array for IRAS biochemical detection is presented. The reflection spectra of the printed gold micro-flake arrays with various lengths and periods have been measured and compared with simulation results using COMSOL. And then, the printed plasmonic

substrates are characterized for plasmonically-enhanced IRAS biochemical detection of BSA. The performance of this substrate is presented in detail.

Chapter 5: Summary and outlook. In this chapter, conclusions are made on this project and the future work to be continued on plasmonic sensors is also presented.

Chapter 2

Precision photoreduction technology for direct printing of plasmonic micro/nano-structures

2. 1 Introduction

Nowadays, advances in fabrication technologies have pushed the progress in plasmonics. For example, in terms of SPR biosensors, when compared with the thin film metal structures used in the 1980s [46], ordered nanohole arrays or other well-defined metallic structures have been achieved using modern fabrication technologies [47-49]. Their strong and controllable optical signal enhancement is extremely suitable for biosensing applications.

To make LSPR biosensors, metallic nanoparticles were widely prepared through chemical synthesis and then deposited on a substrate to form plasmonic devices [50]. Such a process can efficiently prepare metallic nanoparticles with a controlled size and even geometry. However, a further process need applied to pattern these nanoparticles on a substrate to make plasmonic sensors. By exploiting the geometry of nanoparticle arrays and other planar nanostructures, plasmonic extinction spectra with intense, narrow resonances can be designed. Using innovative lithography methods, various metallic structures have been fabricated, like nanohole arrays in gold films [51], periodic gold nanorings arrays [52], and plasmonic gold mushroom arrays [21].

Moreover, progress in fabrication techniques allows the observation of collective oscillations in plasmonic systems supporting localized surface plasmon resonances which are then called surface lattice resonances. In arrays of metallic nanostructures, their quality factors of surface lattice resonance can be tailored up to even several thousand which are 3 orders larger than that of a localized surface plasmon resonance of an isolated metallic nanoparticle [53]. Some conventional micro/nano fabrication technologies for these plasmonic structures are introduced below including their advantages and drawbacks.

2. 2 Conventional micro/nanofabrication technologies for plasmonic structures

a) Electron beam lithography

Electron Beam Lithography (EBL) is a fundamental nanofabrication technique that can not only directly fabricate arbitrary 2D structures with sub-10 nm feature sizes, but also provide high yields of subsequent transfer of nanopatterns through masks and templates. Therefore, it is one of the most important technologies in nanofabrication.

This direct writing system has the advantage of extremely high resolution and arbitrary patterning preparation without a mask while the drawback is that it takes a lot of time to fabricate large-area complex structures and requires expensive nanofabrication facilities and extra fabrication processes. It is exactly because the characteristics of high resolution and large degrees of freedom of EBL are very

compatible with the processing requirements of plasmonic nanostructures composed of two-dimensional periodic nanostructures that EBL is currently most widely used in the processing of plasmonic metallic substrates. And those substrates fabricated by EBL are widely used in different optical bands and different metal systems (such as silver, aluminium, chromium, and magnesium, etc.) to achieve beam deflection [54], lens focusing [55, 56], holography display [57−60], dynamic metasurface [61−63] and other applications, see **Figure 2.1**.
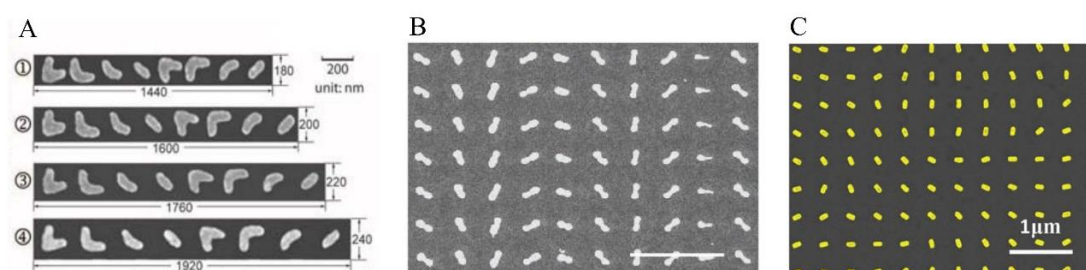
Figure 2.1 SEM images of different plasmonic nanostructures fabricated by EBL. Adapted from Ref [54, 56, 58].

b) Focused Ion Beam

Focused Ion Beam (FIB) etching is one of the most precise maskless micro/nano fabrication methods. Both bottom-up and top-down fabrication processes are available in FIB, which enhances the ability of FIB to precisely fabricate complex 3D micro/nanostructures. By integrating Scanning Electron Microscope (SEM), energy dispersive spectroscopy and other equipment such as a high-precision piezoelectric table, micro/nano manipulator, etc., FIB has become a micro/nano fabrication technology with an extremely high degree of freedom and capability of real-time observation. However, the high cost, the very low processing efficiency, and the limited

size of the processed substrate limit its applications in sample preparation, repair, and small-scale prototype verification. In addition, since the general Ga^+ beam diameter is larger than that of the electron beam, the resolution of FIB is lower than that of EBL.

Taking advantage of its large degree of freedom, FIB is well adapted for discontinuous patterns such as hole or gaps. Sub-5 nm arrays of holes have been obtained in Ref [64], see **Figure 2.2**.
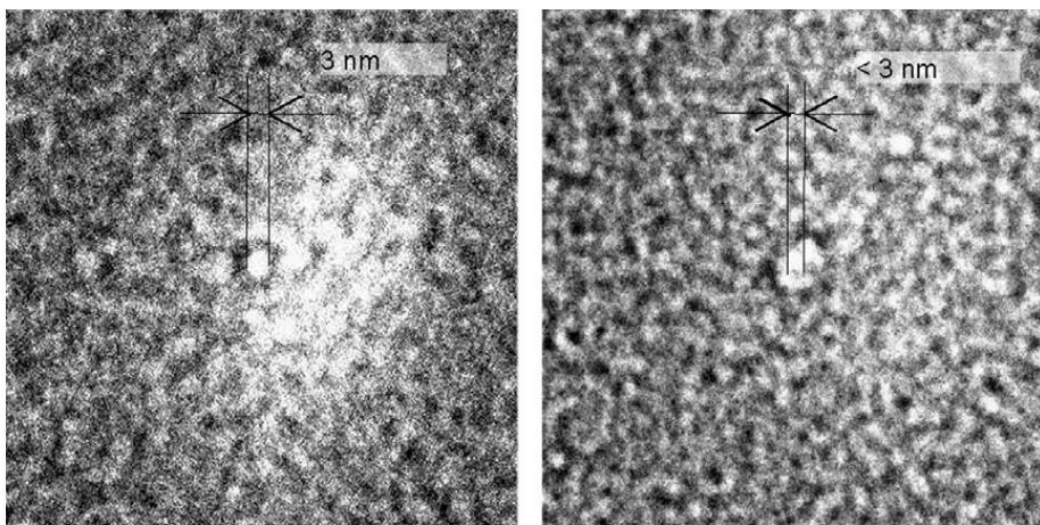
Figure 2.2 50×50 nm transmission electron microscopy images showing nanometre-sized pores (bright) drilled in a 20 nm thick membrane for a same point dose $\sim 10^6$ ions. Adapted from Ref [64].

c) Nanoimprint Lithography

Nanoimprint Lithography (NIL) is a technique which can replicate nanostructures using mechanical deformation. It possesses the advantages of high resolution, large area processing, but it still requires high-resolution equipment to manufacture templates, and it is necessary to remove the residual glue after imprinting by etching, which has certain damage to the glue.

Traditional NIL can be divided into thermal curing and UV curing. Thermal curing

utilizes the characteristics of low viscosity at high temperatures. When the main mold is pressed on the substrate, the polymer coating is cured by heating and then after cooling the template is separated. Therefore, the pattern is transferred to the polymer layer. This process is very simple and can be directly used for the processing of metasurfaces. Another curing method of NIL is UV curing, which uses a liquid polymer spin-coated on the substrate, and UV radiation is applied to cure the polymer during imprinting, which requires that the template should be transparent to UV light. This method eliminates heating and cooling time, improves production efficiency, and can be carried out under the conditions of room temperature and low pressure. Nanoimprint lithography has been demonstrated to print nanowire grid polarizers on flexible substrates. It can even pattern 2.5D structures using only one processing step, see **Figure 2.3**.
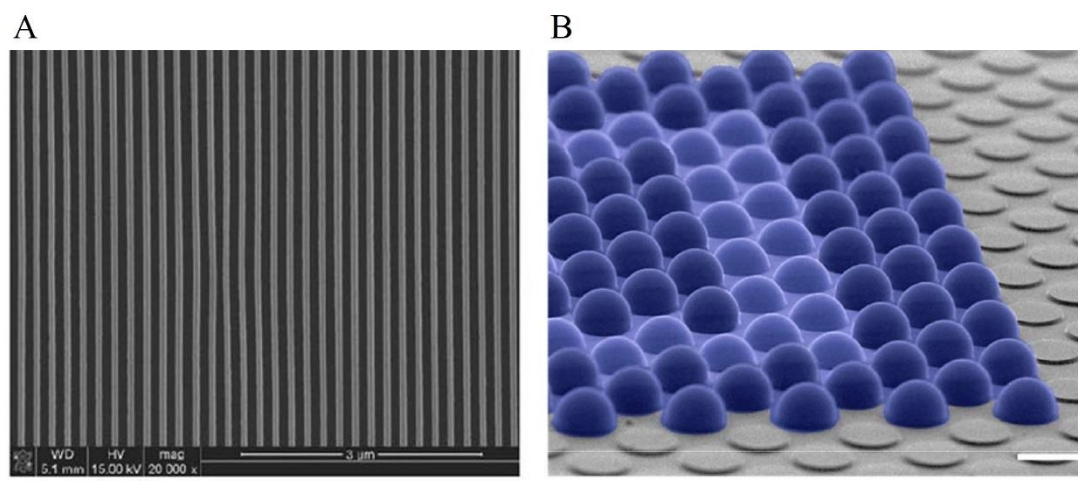
Figure 2.3 SEM images of nanowire grid polarizer (A) and microlens arrays of varying shape (B) fabricated by nanoimprint lithography. Adapted from Ref [65-66].

d) Projection Photolithography

Direct writing techniques such as EBL and FIB have been used to fabricate

plasmonic mettalic substrates with various functions. However, their fabrication process is based on a point-by-point scanning method, which requires a lot of processing time and high processing costs for the preparation of large-scale nanostructures, so it is not suitable for mass production. In contrast, Projection Photolithography (PPL) is a technology that transfers the well-designed pattern on the mask to the substrate with the help of photoresist. In this techniques, ultraviolet light is irradiated on the substrate with photoresist through the mask in a stepping or scanning manner, and the exposed area of the photoresist undergoes a chemical reaction: the exposed area (positive photoresist) or unexposed area (negative photoresist) is removed after developing. And then etching technology is used to process patterns on the substrate, which effectively shortens the exposure time. Therefore, such technique is one of the most suitable technologies for mass production of large-area plasmonic mettalic substrates, and it is promising to move them from the laboratory to mass production applications. A typical plasmonic structure fabricated by PPL is presented in **Fig. 2.4**.
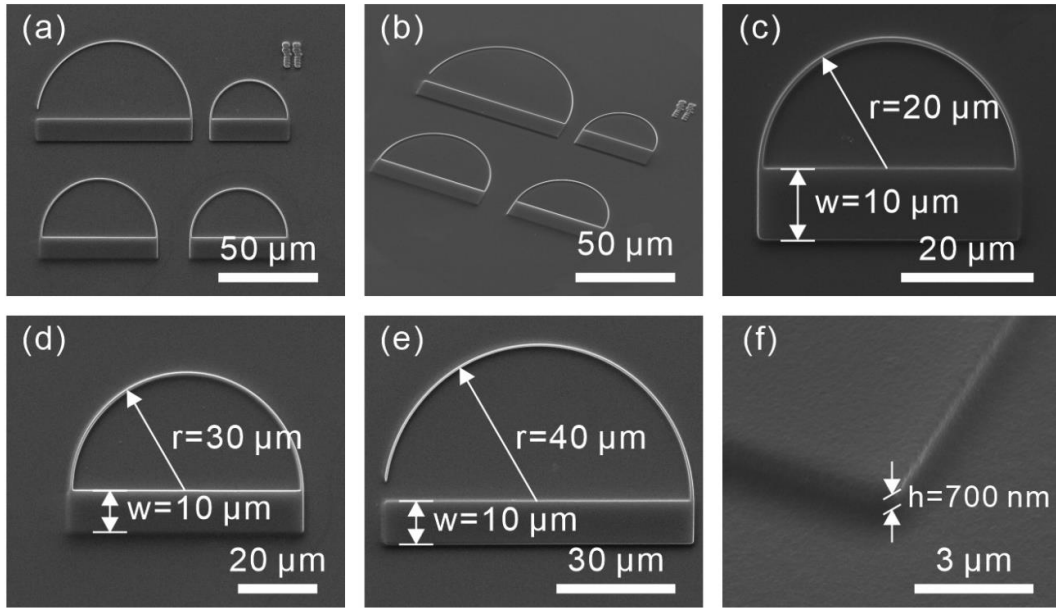
Figure 2.4 SEM images of integrated photonic surface structures composed of a dielectric semicircle ridge and a dielectric block fabricated by PPL. Adapted from Ref [67].

2.3 Precision photoreduction technology

Based on previous discussions, it is clear that significant progress in the micro/nano fabrication techniques has been made in recent years. However, these fabrication technologies cannot fulfil the daily growing need that a direct, rapid and cost-effective fabrication technology with control over the geometries of plasmonic structures is highly desirable to make full use of the potential of the unique property of LSPR. Most of the current fabrication technologies can only meet part of these demands. For example, EBL, one of the most popular nanofabrication technologies, possesses the great ability to precisely fabricate plasmonic nanostructures with well defined geometries. Benefiting from this technology's high resoulution, plasmonic metamaterials with novel optical properties have been developed and demonstrated to various applications like color generation [68]. However, this outstanding performance is based on the expensive nanofabrication facilities and extra fabrication processes are

43

needed which limits its usage to certain areas such as research and prototype devices. Moreover, many other techniques also suffer from this tradeoff between precision and throughput.

Therefore, to meet these demands, a precision photoreduction technology is developed by Y. Zhang et al. which can directly print plasmonic structures of gold/silver nanoparticles in a cost-effective way [69, 70]. Moreover, the ability of this technology to rapidly fabricate plasmonic structures with precisely size-controlled gold/silver nanoparticles in a unique one-step fabrication process makes it quite suitable for the further development of plasmonic devices.

This technology is based on the photocatalytic reduction reaction upon on a thin TiO_2 layer, with which electrons can be excited to the conduction band from the valence band when irradiated by UV light. Due to this electron-hole separation, metal ions can be transferred to metal elements on the surface of TiO_2 film and thereby produce metal nanoparticles under the control of UV exposure dose related to the light intensity and exposure time. Thus, it can also be called as an additive printing technology. The following equations are used to describe this interaction for the growing of gold/silver nanoparticles:

$$TiO_2 \xrightarrow{h\nu} TiO_2(h^+) + e^- \qquad (2.1)$$

$$Au(SC(NH_2)_2)_2^+ + e^- \longrightarrow Au(s) + 2SC(NH_2)_2 \qquad (2.2)$$

$$Ag^+ + e^- \longrightarrow Ag(s) \qquad (2.3)$$
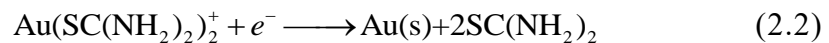
To achieve this additive printing technology, a self-developed ultraviolet(UV) lithography system is utilized. UV(365 nm) beam generated from the light source

illuminates onto the DMD chip. The reflected light is modulated to generate UV patterns which are previously uploaded to the DMD chip. And then, the UV patterns will be finally projected on the substrate after passing through the projection optics. The excited electrons then interact with metal ions leading to the generation of metal nanoparticles upon the TiO_2 film surface.

There are several merits of using such a DMD-based exposure system. First, the DMD is a high-speed electronic device with two main states, on state and off state. The on state means that the reflected light beam will irradiate on the surface of the substrate. In contrast, when the DMD is in off state, the reflected light beam cannot be collected by the projection optics. Therefore, a rapid generation and switching of UV patterns are achieved and controlled by the predefined time sequence. Moreover, a DMD chip contains millions of pixels. Each pixel is around 300 nm and can be controlled independently which means the exposure dose in each pixel is in precise control.

2. 4 Direct printing of plasmonic patterns of size-controlled AuNPs

The fabrication process for the structures formed by size-controlled AuNPs includes the following steps. Firstly, the substrate is spin coated to get a TiO_2 film. Normally, when exposed to the same exposure dose, the thicker the TiO_2 film is the larger the gold nanoparticles are. However, due to the FP cavity effect caused by the TiO_2 layer, it is better to use a very thin TiO_2 layer (Thickness < 20 nm) to obtain a clear LSPR peak. Secondly, a glass container was made to contain the growth solution and provide a flat

liquid surface. $HAuCl_4$ solution, CH_4N_2S solution, $C_4H_{12}KNaO_{10}$ solution, DI water, and $C_6H_9Na_3O_9$ solution were used to prepare the growth solution (1:1:1:1:4). Modulated UV light by uploaded patterns was then projected on the surface of the substrate using our DMD-based exposure system. During exposure, a certain pattern was formed with AuNPs growing toward target size. However, these fabricated AuNPs are normally agglomerates of smaller particles, see **Fig. 2.5 (a)**. This can be understood by the complicated dynamic behaviours of AuNP growth kinetics that the initially produced AuNPs can influence the movement of generated electrons and thus agglomerates of smaller AuNPs are formed. A widely used method – thermal treatment is utilized to reshape the AuNPs. Our sample is heated at 450 °C for 2 hours to reshape AuNPs to more regular shape. After thermal treatment, these AuNPs become more compact and spherical, and the surface of AuNPs became smoother, see **Fig. 2.5 (b)**.
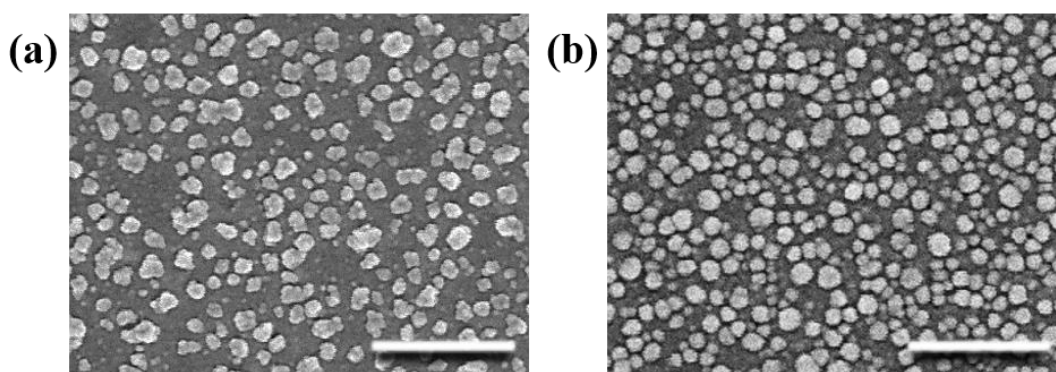
Figure 2.5 SEM images of the AuNPs (a) before and (b) after thermal reshaping at 450 ℃. The scale bars are 300 nm.

One of the merits of this photoreduction technology is the ability to fabricate size-controlled AuNPs. In **Fig. 2.6 (A)**, when the exposure dose is increased from 47.276 J/cm^2 to 283.65 J/cm^2, the size of the AuNPs (with thermal reshaping process) gradually increases from ~23 nm to ~46 nm. A near linear relationship between the size of AuNPs

and exposure dose is shown in **Fig. 2.6 (B)**. Moreover, when using a higher exposure

dose small AuNPs around these relatively larger AuNPs can merge into relatively larger

AuNPs after thermal reshaping. That's why there are some irregular AuNPs appear

when using higher exposure doses, see **Fig. 2.6 (A iii, iv)**.
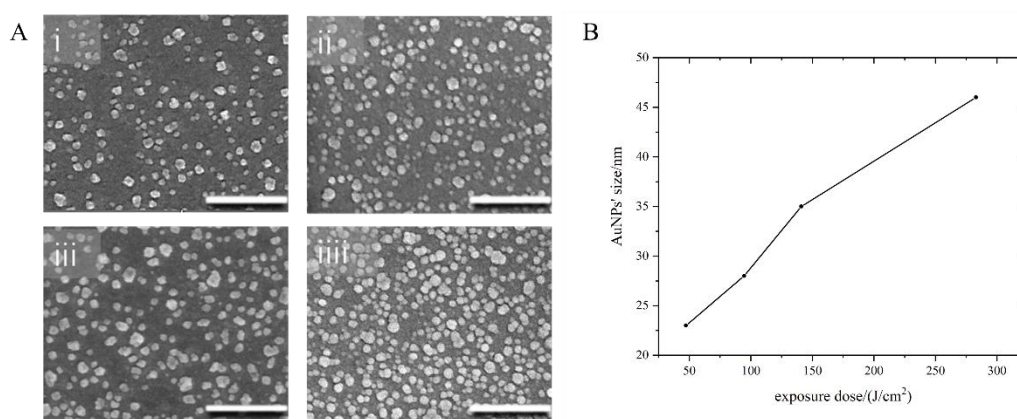
Figure 2.6 (A) SEM images of the AuNPs of different size printed with different UV
exposure doses. The scale bars are 300 nm. (B) The relationship between gold NPs' size and
exposure dose.

Fig. 2.7 shows microscopic images of three types of micropatterns of gold

nanoparticles printed on a TiO_2/SiO_2 substrate using different exposure doses. All the

samples were thermally treated at 450 ℃ for 2 hours. These microscopic images of

AuNPs micropatterns were taken from the AuNPs side, and they showed different

colours. With the increase of exposure doses, the size of fabricated AuNPs gradually

increases and their colours viewed from the AuNPs side change from light blue to dark

red. Therefore, this indicates the red shift of LSPR peaks of these printed AuNPs.

Moreover, normally these printed micropatterns of AuNPs were fabricated within 5

mins. In this case, a rapid and cost-effective fabrication method is achieved by precision

photoreduction technology.
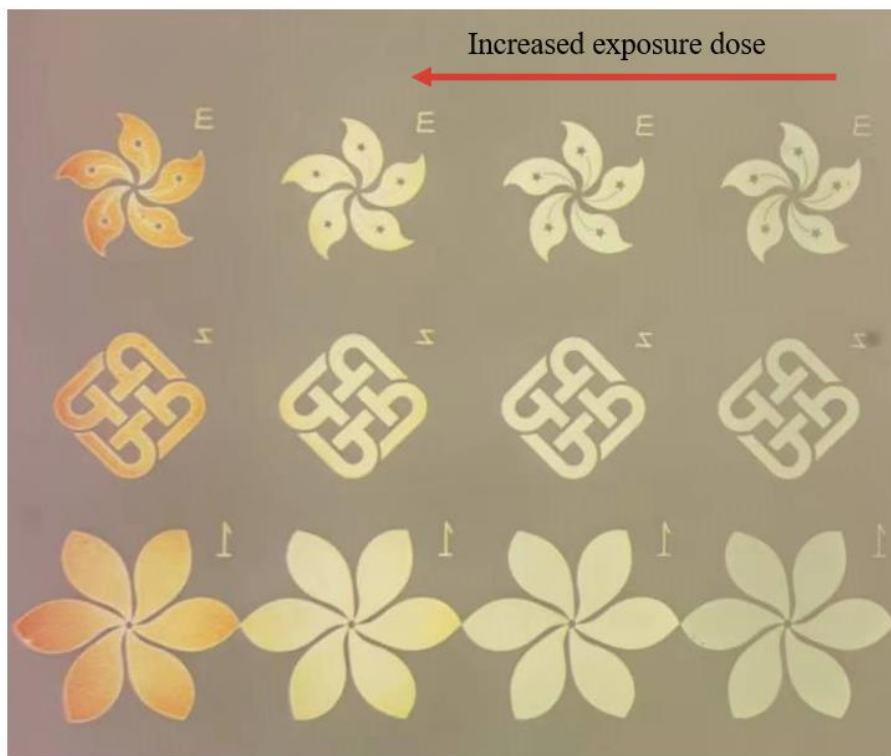
Figure 2.7 Microscopic images of the printed plasmonic patterns of AuNPs with different UV exposure doses.

Chapter 3

Optical fiber-tip plasmonic biosensors based on directly printed size-controlled AuNPs

3. 1 Introduction

As a powerful tool, LSPR is widely utilized in chemical and biological sensing experiments. It is an optical phenomenon originated from noble metal nanostructures. The incident light can interact with the free electrons within the metal nanoparticles resulting in this phenomenon [71]. Noble metals including silver and gold are commonly used materials and their LSPR peak wavelengths are normally in the visible range [72]. Among these materials, the sharpest and strongest spectrum is found in Ag. However, Au is most commonly used in biological applications due to its biocompatibility [73].

Since the LSPR wavelengths of metallic structures are influenced by the surrounding environment, once there are changes in the surrounding environment they could be sensed. These changes will lead to the spectral shifts of extinction spectra which can be used to detect many organic molecules. Moreover, the highly localized electromagnetic field can enhance spectral information for applications including SERS, and SEIRAS.

Normally, biosensors based on LSPR of noble metal nanostructures are fabricated on the silica glass slides. EBL, nanoimprinting lithography and many other conventional

nanofabrication technologies have been utilized to fabricate various metallic nanostructures on glass slides. However, for these nanostructures, their measurement setup is quite complicated and bulky which needs the optical microscope and optical alignment apparatus. Therefore, traditional LSPR sensors constructed on glass slides have difficulties in practical applications rather than laboratory research when considering these limitations, such as the difficult sample handling process and the requirements for expensive desktop apparatus.

To overcome these limitations, research efforts have been put into coupling LSPR sensing and fiber optic technology which creates the so-called LSPR optical fiber sensors [74-76]. Optical fiber is a perfect carrier for the transmission of light and it offers several advantages compared to other substrates, such as small size, high mechanical strength and flexibility. Moreover, the optical fiber tip is a unique and natural substrate. We can expect a direct interaction between incident light and plasmonic structures on the optical fiber-tip. The combination of optical fiber and metallic plasmonic nanostructures makes the entire biosensing system smaller and easier for measurement outside the laboratory environment. In addition, LSPR-FO can provide other benefits such as biocompatibility, all-optical interrogation, low-cost, and multi-channel performance capabilities required for high-throughput applications. Since the metallic plasmonic nanostructures are located at the fiber tip above the core, no optical alignment is required between the sensors and the test environment. Therefore, the shortcomings corresponding to traditional LSPR sensors, such as the use of bulky and complicated measurement setup, are solved. This makes LSPR-FO

biosensing technology suitable for point-of-care and many other applications.

3. 2 Design and analysis of optical fiber-tip plasmonic sensors
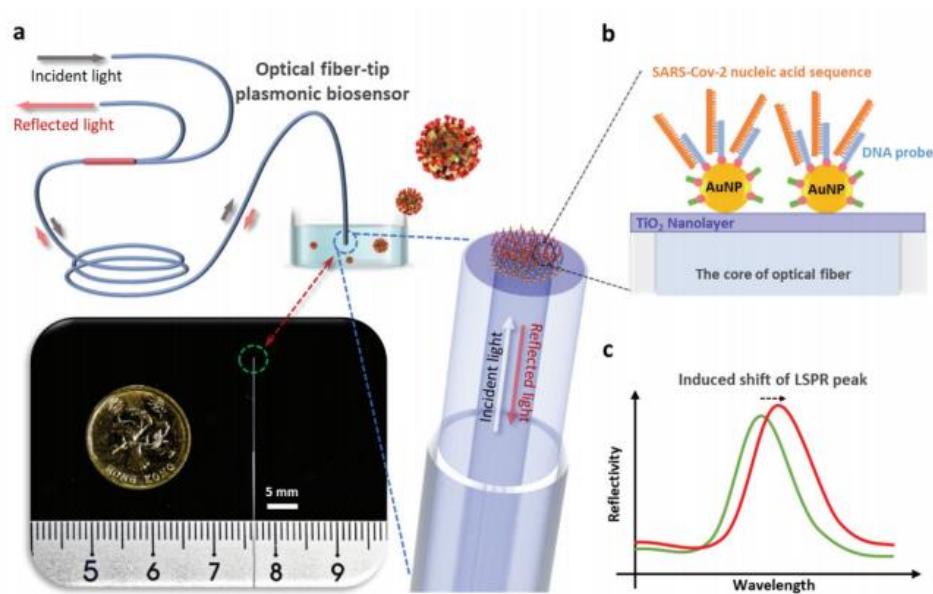
Figure 3.1 Schematic and working principle of optical fiber-tip plasmonic biosensor. (a) Schematic of the fiber-based plasmonic biosensor; (b) Schematic structure of the sensing part of the AuNPs-based plasmonic biosensor; (c) Working principle of the plasmonic biosensor.

The structural design and working mechanism depicted in **Figure 3.1**. By using the precision photoreduction technology the Au nanoparticles are selectively printed on the cleaved fiber end surface as shown in **Figure 3.1 (a)**. As a consequence, the reflection spectrum will have a maximum when at the plasmon resonant frequency. As mentioned in **Chapter 1**, the LSPR peak wavelength can be used for the sensing of refractive index variations which can result in the shift of the LSPR peak wavelength. According to this principle, when the sensor is immersed into a liquid containing target molecules which will be adsorbed by the Au nanoparticles as shown in **Figure 3.1 (b)**, at different

concentrations the liquid's refractive index is changed accordingly which can be detected through the LSPR peak as shown in **Figure 3.1 (c).**

3. 3 Fabrication of optical fiber-tip plasmonic sensors

In the fields of LSPR sensing, Au is often chosen to fabricate metallic nanostructures with favourable properties like inert nature and biocompatibility. Based on the precision photoreduction technology as mentioned in **Chapter 2**, AuNPs-based micropatterns have been printed on the optical fiber tip.

During the fabrication process, a 2% TiO_2/IPA solution is used to spin-coat a TiO_2 nanolayer upon the end surface of a multimode optical fiber, which was polished by using a commercial optical fiber end-surface polishing machine. The typical parameters for the spin-coating method are 500 rpm/2 s and 3000 rpm/30 s. After baking, the optical fiber with TiO_2 nanolayer is fixed and the gold salt solution is dropped on the top of fiber surface covered by a glass slide. Then, the sample is precisely aligned to the target position for optical exposure using an in-house digital UV lithography setup as shown in **Figure 3. 2**. Finally, with a sliced image data of the designed pattern, the UV light is modulated and the AuNPs are thus fabricated at specific regions according to the formed UV pattern. Typically, the exposure time is around 400 s with the UV light intensity of 1803 mW cm^{-2}.
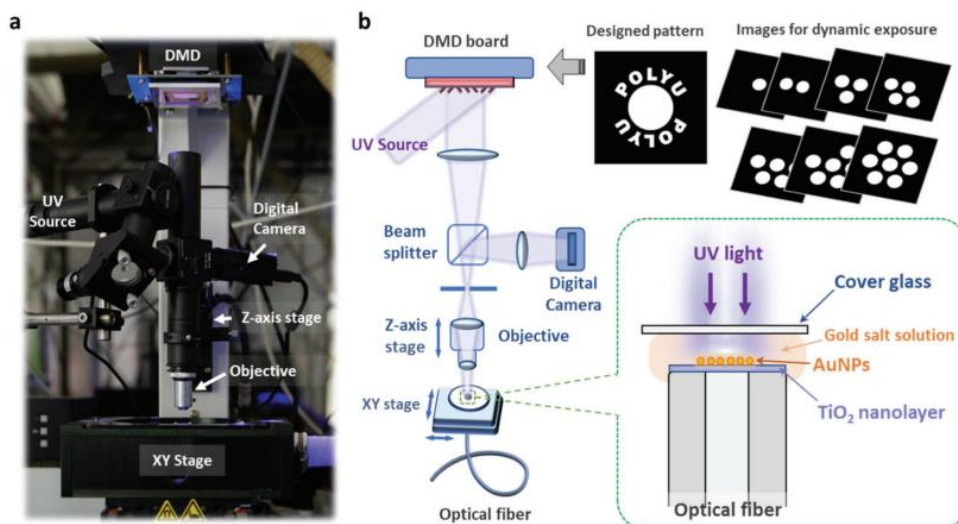
Figure 3.2 Experimental setup and the schematic of fabrication technology. (a) Photo of the in-house digital ultraviolet exposure setup. (b) Schematic of the *in-situ* precision photoreduction technology for fabrication of AuNPs.

After exposure, the optical fiber tip is heated at 450 ℃ to reshape AuNPs into more regular geometry. Since silica can withstand very high temperature, i.e., ~ 1700 ℃, the thermal treatment has negligible influence on the coating-removed silica multimode optical fiber. As shown in **Figure 3.3**, samples before and after reshaping are presented. The AuNPs before reshaping have rough surfaces which become smooth after being treated at 450 ℃ for around 2 hours.

We have prepared four different patterns during the fabrication process and the results are presented in **Figure 3. 4 (a)**. These fabricated samples illustrate the ability of this precision photoreduction technology to selectively print AuNPs with designed patterns. In later demonstrations of the detection of antibody and DNA sequence, to achieve the largest sensing area the pattern of our university name and a centre circle with the same diameter with the multimode fiber's core is adopted.
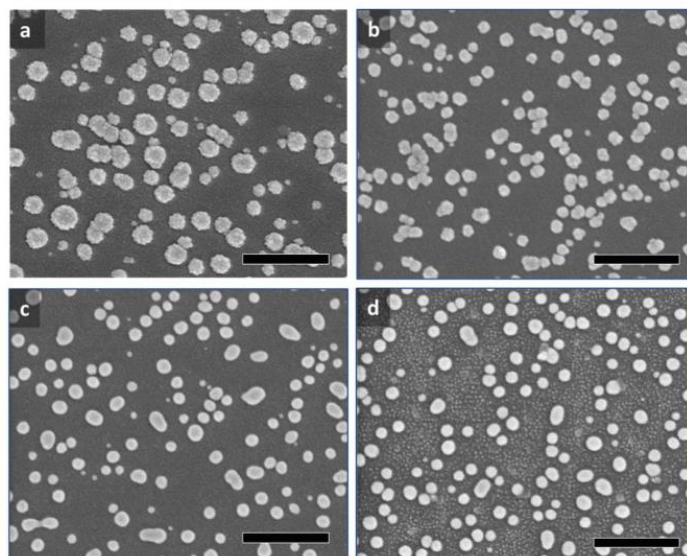
Figure 3.3 SEM images of the AuNPs before and after thermal reshaping treatment. (a) SEM image of the AuNPs before thermal treatment; (b,c,d) SEM images of the AuNPs after thermal treatment at 200 °C, 300 °C and 450 °C, respectively. All scale bars are 500 nm.

Another key parameter for the fabrication of AuNPs is the optical exposure dose. In this precision photoreduction technology, it has the ability to tailor the size of AuNPs by the optical exposure dose. With different optical exposure doses, various sizes of AuNPs are obtained, see **Figure 3. 4 (b)**. Small and relatively circular AuNPs are printed when using a small optical exposure dose while some large and noncircular AuNPs appear with the increase of the optical exposure dose.

The reflection spectra of the printed micropatterns of AuNPs to solutions with different refractive indexes are measured firstly using a 3dB broadband fiber-coupler, an optical spectrum analyzer and a broadband light source. Here, we presented two sensors with different geometries after being tested and their reflection spectra are presented in **Figure 3.4c (i, ii)**.
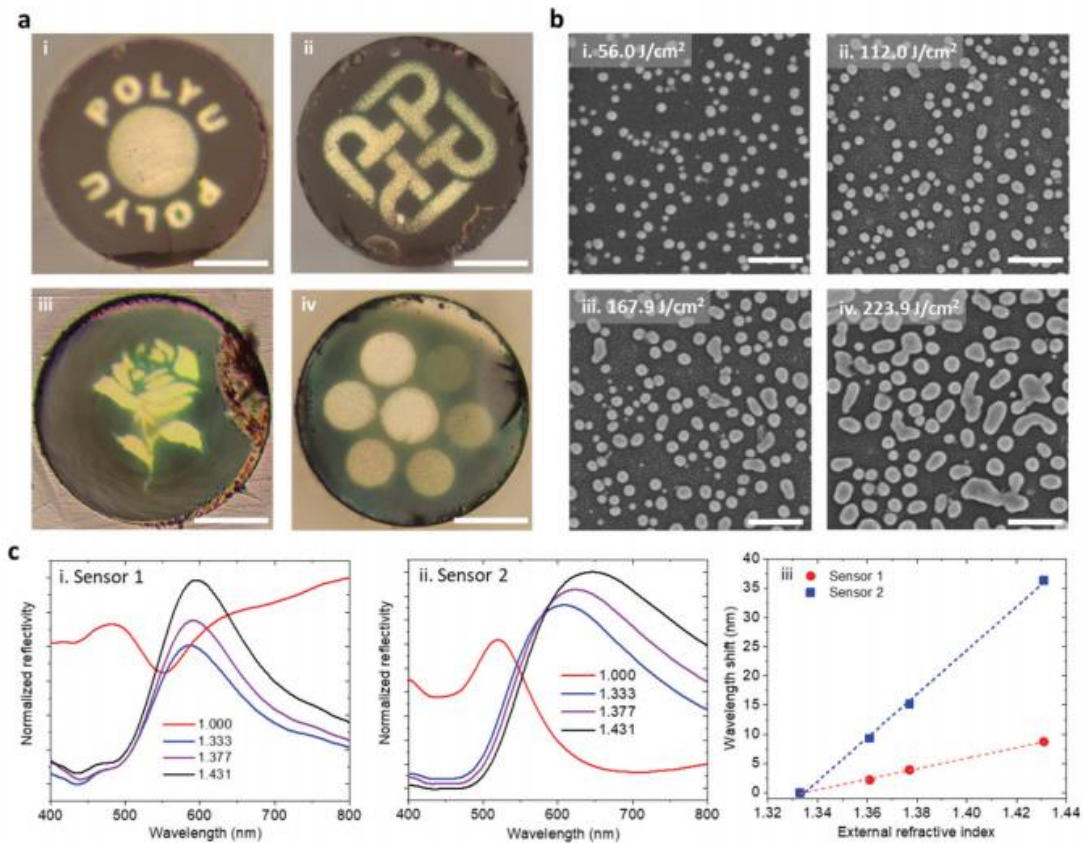
Figure 3.4 Microscopic images of the printed AuNPs and the reflection spectra of the sensors. (a) Optical microscopic images of the printed micropatterns of AuNPs on optical fiber end-face. i & ii. University name and logo; iii. Flower; iv. Circles with AuNPs of different sizes. The scale bars are 40 μm. (b) SEM images of the AuNPs of different size printed with different UV exposure doses. The scale bars are 400 nm. (c) Measured reflection spectra of the sensors: i. Sensor 1 based on 70-nm AuNPs; ii. Sensor 2 based on 100-nm AuNPs; iii. Spectral responses of the two sensors to the change of external RI.

For sensor 1 (70nm AuNPs), there is a spectral dip in the reflection spectrum when it is put in the air. This spectral dip mainly results from the F-P cavity formed by the TiO₂ layer which dominates the reflection. Scatterings from the gold nanoparticles of small size are thus suppressed. In terms of sensor 2 (100 nm AuNPs), stronger scatterings from them offer a clear LSPR peak at around 520 nm when sensor 2 is put in the air. To investigate the relationships between their LSPR peaks and the surrounding refractive index, these two sensors are immersed into solutions with different refractive indices, see **Figure 3.4c (iii)**. A higher sensitivity is found in sensor

2 which is 371.0 nm/RIU. But, the LSPR peak of sensor 2 is broader and thus it has a poor spectral resolution which is not good for the LSPR based sensing applications.

3. 4 Detection of goat anti-human immunoglobulin G (IgG)

The fabricated optical fiber-tip plasmonic biosensors with better optical resolution in LSPR peak are selected first by refractive index testing. These samples with sharp LSPR peaks in reflection spectra are used for the detection of the target antibody. **Figure 3.5 (a)** shows the modification processes for the detection of goat anti-human immunoglobulin G (IgG). First, the AuNPs are treated by cysteamine (Sigma Aldrich Inc, 5 mM) and glutaraldehyde (Sigma Aldrich Inc, 1 wt% @) for 1 h and 30 min at 20 °C, sequentially. After that, the sample is immersed into human IgG/PBS solution (Sangon Biotech (Shanghai) Co., Ltd., 10^{-7} M) for 2 h at 20 °C, during which the human IgG antigen is immobilized upon the AuNPs inducing the biosensor's LSPR peak shifts to longer wavelength, see **Figure 3.5 (b)**. The relative positions of LSPR peaks at three typical time are plotted in the inset figure. The last step for the functionalization of the biosensor is that the Serum albumin protein (BSA) (Sigma Aldrich Inc, 1 wt% in PBS) is used as a blocking agent for 1h at 20 °C.
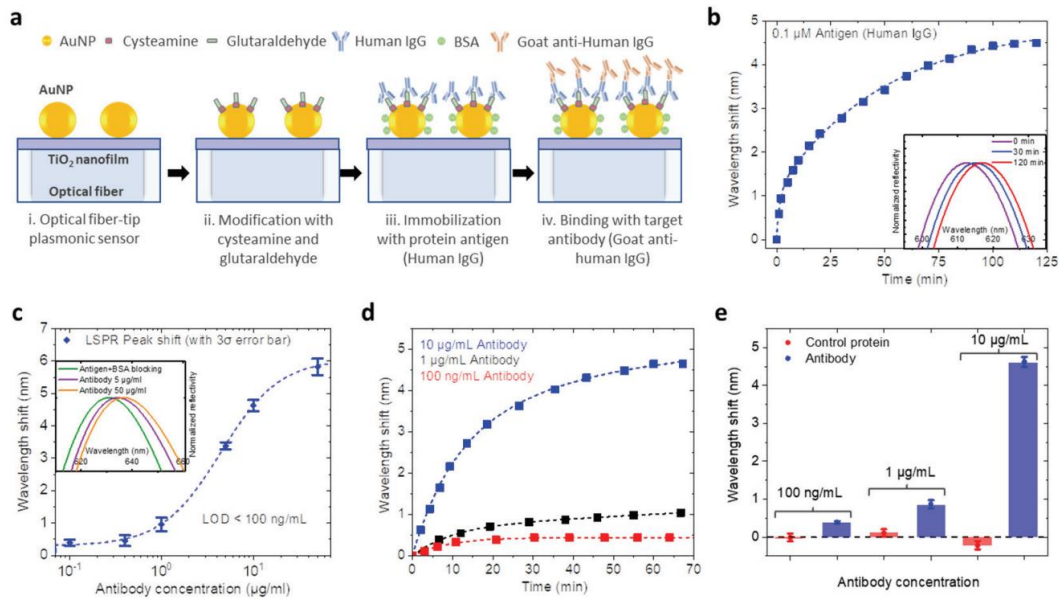
Figure 3.5 Detection of goat anti-human immunoglobulin G (IgG). (a) Schematics of surface functionalization and antibody detection principle. (b) Wavelength shift of the biosensor's LSPR peak of the biosensor during the functionalization with antigen, i.e. human IgG. (c) Responses of the biosensor to different concentrations of target antibody, i.e. goat anti-human IgG. (d) Dynamic response of the biosensor to the target antibody solutions of different concentrations. (e)Specificity testing result by comparing the responses to the antibody and control protein BSA.

Different concentrations of target antibody are used for the sensor's performance's and responses' characterizations as given in **Figure 3.5 (c)**. The inset figure demonstrates the interaction between gold nanoparticles and the target antibody from which it is clear that the higher concentration of the target antibody the larger shift of the LSPR peak. The calculated LOD is <100 ng/mL. Notably, there is an almost linear response range and the deduced sensitivity in this range is ~0.062 nm/nM.

Response time is another important characteristic of the sensors. **Figure 3.5 (d)** describes the dynamic response of the biosensor to three concetrations of target antibody. It indicates that the 90%-response time of the sensor to the three concentrations of target antibody solutions are 20.5 min, 36.8 min, and 38.8 min, respectively. Moreover, The biosensor's specificity testing has also been performed and

its results are shown in **Figure 3.5 (e)**. Serum albumin protein (BSA) is used as a control protein to compare the biosensor's response to it and the target antibody. A very good specificity of the biosensor can be seen from these results even though the target antibody is at very low concentration.

3. 5 Detection of SARS-CoV-2 mimetic DNA sequence

Stimulated by the severe consequences of COVID-19, biosensors has become an inevitable tool to cope with public health crisises. Therefore, the fabricated biosensor is tested using the SARS-CoV-2 mimetic DNA sequence (Shanghai DNA Bioscience Co. Ltd) to demonstrate its ability for testing of COVID-19.

Figure 3.6 (a) shows the modification processes for the detection of nucleocapsid protein (N-protein) DNA (Shanghai DNA Bioscience Co. Ltd). First, the AuNPs are treated by SH-DNA probe which is N-protein-f receptor (Shanghai DNA Bioscience Co. Ltd, @20 °C for 5 h). After that, the sample is functionalized inducing the biosensor's LSPR peak shifts to a longer wavelength indicated by **Figure 3.6 (b)**. The relative positions of LSPR peaks at three typical time are plotted in the inset figure. The last step for the functionalization of the biosensor is that the 6-mecapto-1-hexanol (MCH, Sigma Aldrich Inc) is used as a blocking agent (@ 20 °C for 1h) to prevent the influences caused by the unbinding region.
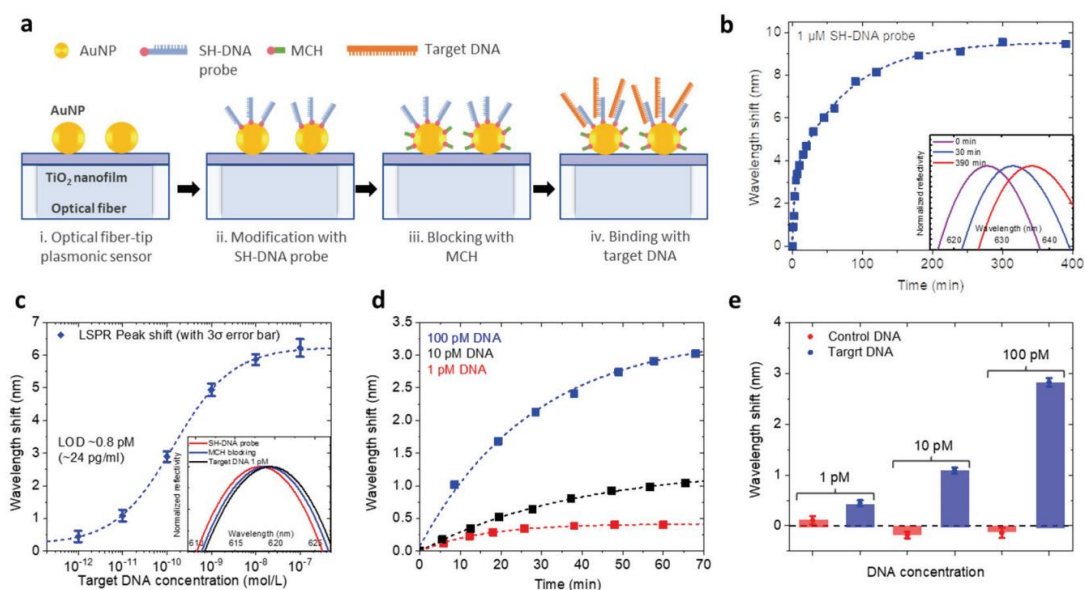
Figure 3.6 Detection of SARS-CoV-2 mimetic DNA sequence. (a) Schematic of the surface functionalization and the nucleic acid testing principle. (b) Wavelength shift of the biosensor's LSPR peak during surface functionalization. (c) Responses of the biosensor to different concentrations of target DNA, i.e., N-protein DNA sequence. (d) Response curves of the biosensor to the target DNA solutions of different concentrations. (e) Specificity testing result of the sensor functionalized with N-protein-f receptor. Target DNA and control DNA are N-protein DNA sequence and Orf1 DNA sequence, respectively.

Target DNA sequence from 1 pM to 100 nM are used for the characterizations of the sensor's performance and its responses are given in **Figure 3.6 (c)**. The inset figure shows the LSPR peak positions after being treated by SH-DNA probe resulting in a red shift of the LSPR peak. The calculated LOD is ~0.8 pM (i.e. ~24 pg/mL). Also, there is an almost linear response range of 1 pM to 100 pM and the deduced sensitivity in this range is ~0.024 nm/pM.

Response time for the detection of the target DNA sequence is also estimated. **Figure 3.6 (d)** describes the dynamic response of the biosensor to three concentrations of the target DNA sequence. 90%-response time of the sensor to target antibody solutions are 32.1 min, 48.9 min, and 49.7 min, respectively. Moreover, the biosensor's specificity

testing has also been performed as shown in **Figure 3.6 (e)**. Orf-1 DNA sequence (Shanghai DNA Bioscience Co. Ltd) is used as control DNA to compare the biosensor's response to it and the target DNA sequence. A very good specificity of the biosensor can be seen from these results even if the target DNA sequence is at a very low concentration.

3. 6 Reusability testing

One of the merits of this optical fiber-tip LSPR sensor is its reusability due to the biocompatibility and inert nature of gold. The biomaterials functionalized on the surface of AuNPs can be chemically removed without damaging the structures each time after using for repeated usage. The experimetal results of the fabricated sensor's reusability using BSA for 8 cycles are presented in **Figure 3.7**. The functionalization of BSA protein leads to the shift of the LSPR peak (**Figure 3.7 (a))**. The LSPR peak positions of the sensor after 8 cycles are presented in the inset figure. It can be seen from **Figure 3.7 (b)** that the LSPR peak can shift to nearly the same position either treated by BSA or chemical removal. Therefore, this kind of LSPR sensor provides the ability to lowdown the cost for the further development of plasmonic devices.
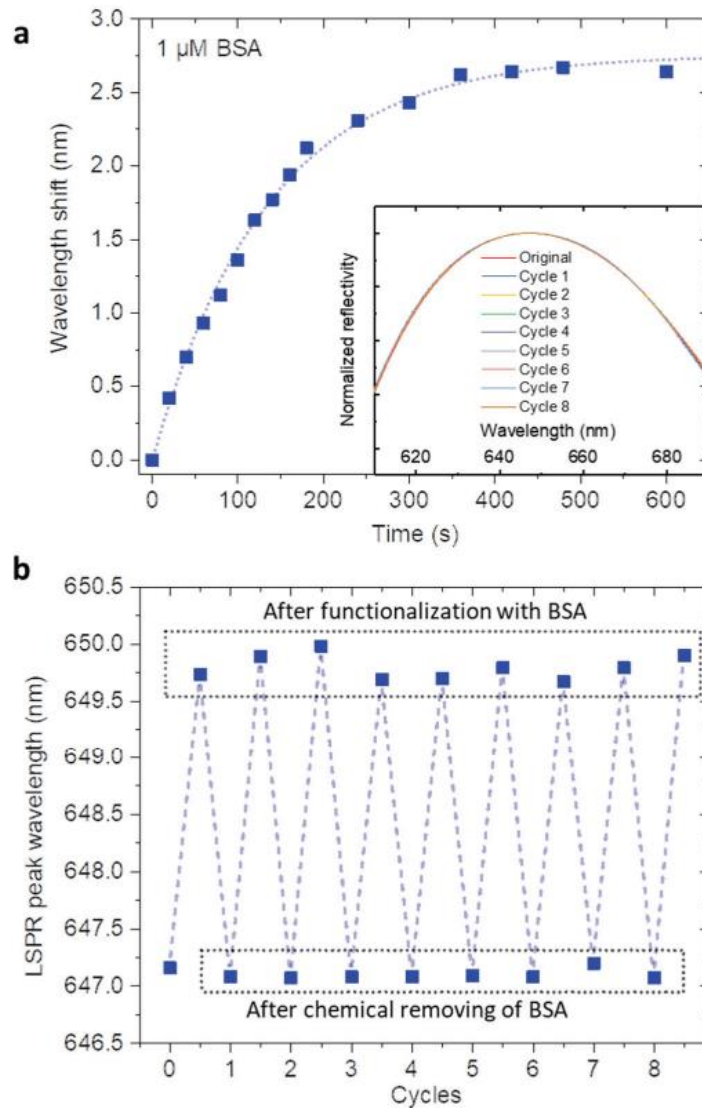
Figure 3.7 Reusability testing result by alternative functionalization with and chemical removal of BSA protein. (a) Measured wavelength shift of the LSPR peak during the functionalization with BSA protein. (b) Repeated shifts of the LSPR peak wavelength in 8 cycles of alternative functionalization with and chemical removal of BSA protein.

3. 7 Summary

In summary, selectively printed AuNPs into micropatterns on optical fiber tip via precision photoreduction technology have been achieved. Their reflection spectra have been characterized at different refractive indices. Moreover, the ultrasmall optical fiber-tip sensor has shown a sensitivity of 0.062 nm/nM to target antibody, and LOD is calculated to be <100 ng/mL. In terms of the target DNA sequence sensing, a sensitivity

of 0.024 nm/pM is obtained. The LOD of the biosensor for the detection of SARS-CoV-2 mimetic DNA is ~0.8 pM which is better than the reported fluorescence methods [77-78]. Remarkably, our sensor's response time varies from 20 to 50 min, which is relatively fast compared with other similar affinity-based biosensors. It may result from the small size of the sensor. For example, the diffusion length of antibody after $10 \sim 30$ min is around 94 - 281 μm, which is greatly larger than either the thickness or lateral dimension of our sensor. Moreover, the light launched into optical fiber for signal interrogation has a power density of 2.7 W/cm^2, which may cause a rise of the local temperature due to photothermal effect and thereby accelerate the sensor's response. Moreover, the tiny size, reusability and remote detection capability of the optical fiber-tip LSPR sensor have made it a promising candidate for biochemical applications where miniaturization is needed.

Chapter 4

Directly printed plasmonic substrate of periodic gold micro-flake array for IRAS biochemical detection

4. 1 Introduction

Infrared absorption spectroscopy (IRAS) is one of the most popular technologies that can reveal the structural information of organic species since most molecules have specific molecular vibration-caused intrinsic optical absorption peak in the infrared wavelength range. However, the relatively low infrared molecular absorption cross-section is usually weak for the accurate determination of minute amounts of materials according to Beer's law [79]. In order to rectify this problem, plasmonically-enhanced infrared spectroscopy based on various well-designed metallic nanostructures, for example, resonant plasmonic antennas with plasmonic resonances matching with analyte's vibrational modes, was proposed to identify enhanced absorption signal of molecular vibrations. Such metallic nanostructure may cause the collective oscillations of electrons, known as LSPR, providing enhanced electric fields on their surface. Therefore, infrared vibrations of molecules on the surface of such structures result in enhanced absorption cross-sections and strong absorption peaks.

Based on this technology, the enhancement can be achieved when a good match between the plasmonic resonance of the structures and the absorption peak of the molecular vibration is achieved. To meet this condition, the plasmonic resonances of

the metallic structures need properly designed by tailoring their shape, size and the period of the structure array. Typically, these structures can be fabricated using electron beam lithography (EBL) to precisely control their geometries. However, it need use expensive facilities and the whole fabrication process is time-consuming which also prevents the fabrication of large-area sample for practical application. To achieve the full potential of this plasmonically-enhanced infrared absorption spectroscopy in sensing applications, a direct, rapid and low-cost fabrication is thus required. In addition to EBL, many other nanofabrication techniques also suffer from some problems. For example, randomly distributed island films can be easily prepared in a large area at low costs using a deposition method [80, 81]. However, they suffer from a relatively lower enhancement factor. Compared with randomly distributed island metal films, nanoantennas with well-designed geometries are of more interest due to the higher plasmonic IRAS enhancement. Methods like colloidal hole mask lithography are developed which are capable of fabricating nanoantennas into designed geometries [82, 83]. But their problem is that the fabricated nanoantennas are randomly distributed. Using other methods, like the nanoimprint technique, the metallic structures can be fabricated in a fast way and on a large scale with the use of a mask. But the mask is mostly fabricated by EBL and thus the whole fabrication process is still slow and cost-intensive [84-86]. A new approach is thus needed for the direct, rapid and low-cost fabrication of metallic structures for infrared absorption spectroscopy biochemical detection.

An alternative approach to solve this problem involves the use of precision photoreduction technology which was proposed by Y. Zhang et al. [69-70]. Directly printing of patterns of size-controlled AuNPs/AgNPs was achieved without the use of a mask. Therefore, such a precision photoreduction technology is of great potential for the direct, fast and low-cost fabrication of gold micro-flake arrays for IRAS biochemical detection. In this chapter, the fabrication and testing of plasmonically-enhanced IRAS biosensors for using precision photoreduction technology to fabricate gold micro-flakes arrays are reported. More specifically, the precision photoreduction technology is utilized to achieve the fine tune of the plasmonic resonances of the gold micro-flakes arrays by tailoring their geometries. The effect of changing the length of gold micro-flakes and the period of the arrays is numerically simulated and compared with experimental results. Moreover, their plasmonically-enhanced IRAS activity with the traditional protein of Bovine Serum Albumin attached to the surface of gold micro-flakes is presented. The performance of this plasmonic substrate is evaluated including the enhancement factor and the limit of detection.

4. 2 Design and analysis of plasmonic substrate of periodic gold micro-flake array

As shown by **Fig. 4.1**, an array of gold micro-flakes with length L and width w is fabricated on the TiO_2/SiO_2 surface. The key parameters in the design of gold micro-flakes arrays are the length L and width w of every gold micro-flake as well as the period P of this array indicated by **Fig. 4.1**. Due to the proximity effect, the smallest

width of every single gold micro-flake that could be achieved is around 1 μm and the shape of the gold micro-flake differs with the designed rectangular and is more like an oval, see **Fig. 4.3 (c)**. Therefore, in simulation the width of the gold micro-flake is fixed as 1 μm to achieve the maximum aspect ratio of the gold micro-flake and the gold micro-flake is modelled as an oval given in **Fig. 4.2** and a commercial software COMSOL is used. The gold micro-flake's near field distribution is presented and at the tip of the gold micro-flake, an enhanced near field is observed with incident light polarized to the long axis of the gold micro-flake. And then, by changing the length of gold micro-flakes and the period of the arrays, their influences on the IR response of gold micro-flakes arrays are discussed below.
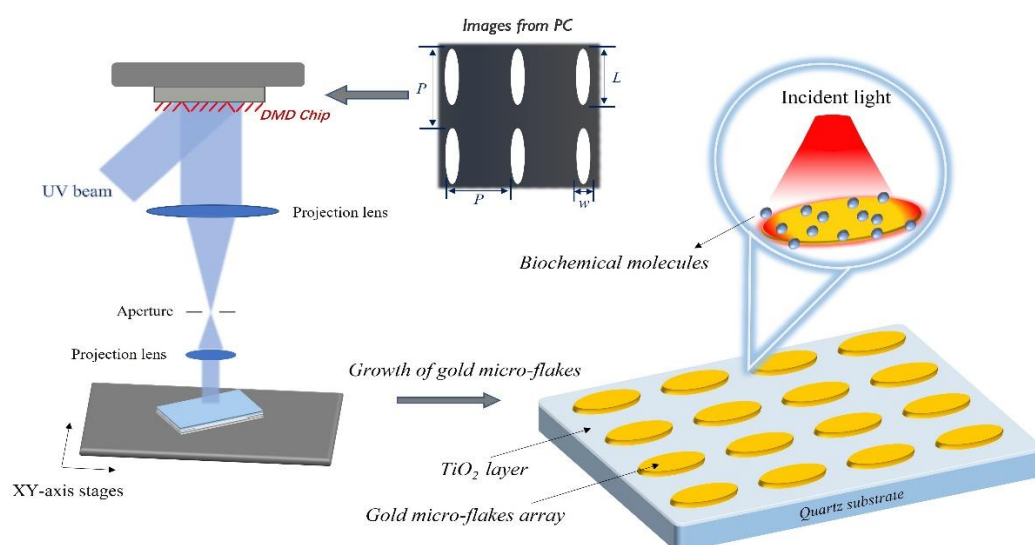
Figure 4.1 Schematic of fabrication technology and the principle of plasmonically-enhanced infrared absorption spectroscopy sensing.

The effect of changing the length L and the separation distance P is firstly described by means of numerical simulation using COMSOL as shown in **Fig. 4. 2**. Polarized light with the electrical field parallel to gold micro-flakes' long axis induces plasmonic resonances in the gold micro-flakes, leading to the appearance of plasmonic resonances

with a peak reflection wavelength that increases with gold micro-flakes' length, see **Fig. 4.2 (b)**. For gold micro-flakes' lengths of 2.1 to 3.0 μm, the resonance wavelength increases with the length of the gold micro-flakes [87,88]. In terms of the period P, with the decrease of it, more closely packed arrays can result in the blue-shift in dipolar coupling between neighbouring gold micro-flakes and broaden resonance peaks [88, 89], see **Fig. 4.2(c)**. Based on these simulation results, the IR response of such a plasmonic device can be tuned by changing the geometries of arrays of gold micro-flakes to match the absorption peak of biochemical materials to achieve the maximum plasmonic IRAS enhancement.
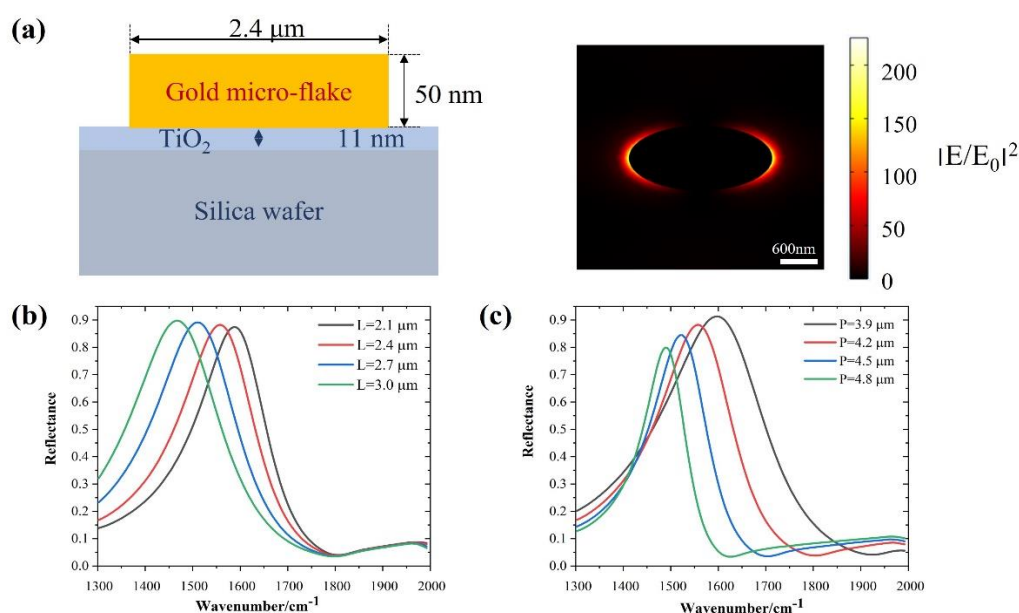
Figure 4.2 Numerical simulations of arrays of gold micro-flakes (a) Simulation model and the calculated electric field enhancement distribution; Simulated effect of changing (b) length L of gold micro-flakes and (c) periodic P of gold micro-flakes arrays.

4.3 Fabrication of the plasmonic substrate of periodic gold micro-flake array

Fig. 4.1 demonstrates the fabrication process of gold micro-flakes arrays. The

substrate was prepared by spin-coating TiO$_2$/IPA solutions on quartz plates (500 rpm/ 5 s+ 4000 rpm/ 30 s) and was then reversely put on a glass container. A silver salt solution with silver nitrate diluted in ethylene glycol (weight ratio 2 : 100) was injected into the space between the surfaces of the substrate and the glass container for the printing of silver-based micro-flake to enable a higher resolution. Our DMD-based UV exposure system was used to print micro-flakes formed by AgNPs. During exposure, due to the photocatalytic reaction, the TiO$_2$ layer can interact with the incident photons resulting in the generation of electrons, which react to silver ions and silver nanoparticles are thus formed; the longer the illumination continues, the larger the AgNPs are. The typical exposure time for micro-flakes was varied from 4 to 7 mins (UV LED's power density 1597.22 mW/cm^2) depending on their geometries. After the growth of silver nanoparticle-based micro-flakes, the samples were immersed in chloroauric acid/hydroxylamine solution (volume ratio 1 : 1) for 10 mins to transfer them into gold micro-flakes. Finally, the sample was baked at 350 °C @ 5 mins to merge the gold nanoparticles inside the gold micro-flakes to obtain smooth surfaces and improve their conductivity. As a result of the fabrication process based on precision photoreduction technology, the gold micro-flake arrays were fabricated, see **Fig. 4.3**.
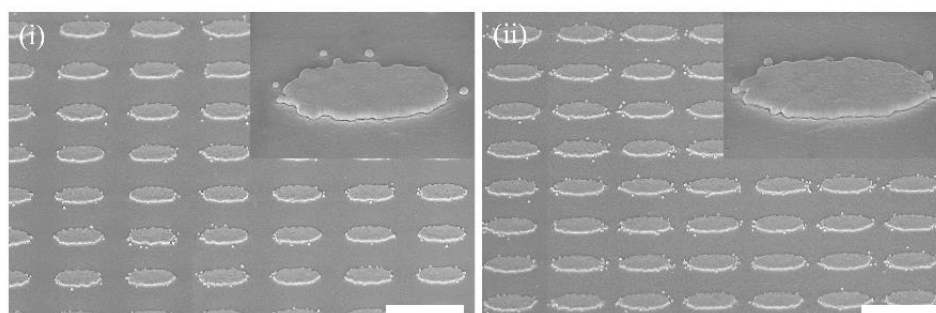
Figure 4.3 SEM images of the directly printed gold micro-flakes arrays with different lengths of (i) 2.1 μm and (ii) 2.4 μm. The scale bar is 4 μm.

4. 4 Testing of the fabricated plasmonic substrate

4. 4. 1 Spectral response of periodic gold micro-flakes arrays

An IR microscope (Bruker Hyperion 1000) was used to measure the plasmonic substre's IR response at normal incidence with NA = 0.52. A bare gold mirror was used as a referrence. All spectra were acquired with 256 scans at a resolution of 2 cm^{-1} from 1300 to 2000 cm^{-1} (5.0 - 7.7 µm). The IR beam passes an IR polarizer (before the sample) aligned parallel to the long axis of gold micro-flakes. The FTIR reflection measurement results of gold micro-flake arrays are as shown in **Fig. 4.4.** With the increased length of gold micro-flakes, the structure's collective plasmonic resonance shifts to a longer wavelength which is in good agreement with simulation results. When modifying the periods of gold micro-flakes arrays, with the increase of it, the peak wavelength of the structure's IR reflectance spectra shifts to a longer one. However, the line widths of the IR reflectance spectra show modest changes. This can be attributed to the relatively large aspect ratio of gold micro-flakes.
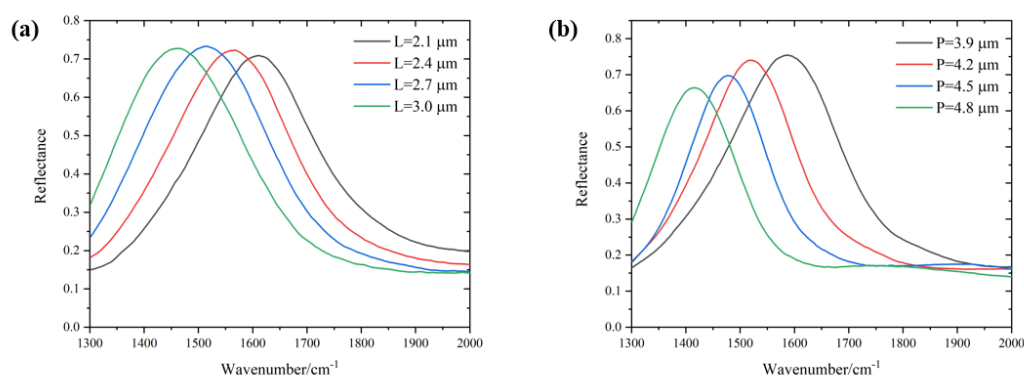
Figure 4.4 Experimental results of IR reflectance spectra by changing (a) length L of gold micro-flakes and (b) periodic P of gold micro-flakes arrays.

4. 4. 2 Results of plasmonically-enhanced IRAS biochemical detection

The plasmonically-enhanced IRAS biochemical detection was achieved. Standard protein–bovine serum albumin (BSA) with amide bands at 1660 cm^{-1} and 1550 cm^{-1} was utilized. Here, the sample was firstly treated under O_2 plasma (200 W, 30s) using a plasma asher. Then the treated gold micro-flake arrays were incubated in a 1 μM BSA solution for 2 h at 30 °C.
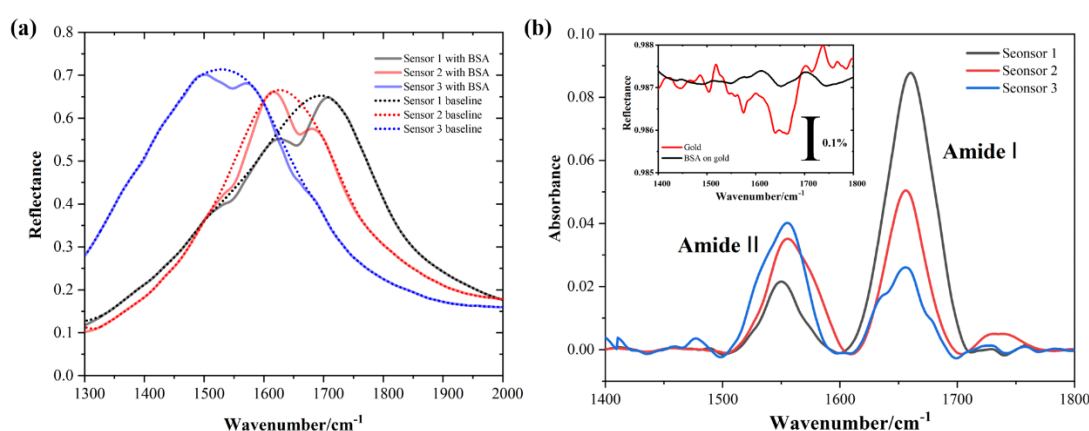
Figure 4.5 (a) Relative IR reflectance spectra of gold micro-flakes arrays covered with BSA. The incident light is polarized along the long axis of gold micro-flakes. (b) Difference absorption spectra of gold micro-flakes arrays.

Gold micro-flakes arrays with different lengths were prepared. Their resonance wavelengths were located at 1530, 1627 and 1689 cm^{-1}, see **Fig. 4.5 (a)**. In these reflection spectra (solid lines), absorption from the BSA protein caused dips in the reflection spectra. As expected, arrays with different resonance wavelengths demonstrate different signal intensities due to the differences in resonance matching between plasmonic resonances and BSA absorption bands. In order to investigate this interaction, the extracted enhanced vibrational signals from the baseline-corrected IR spectra are presented, see **Fig. 4.5 (b)**. It is clear that when the resonance wavelength

shifts from 1530 cm^{-1} to 1689 cm^{-1} the vibration signals of amide-II decrease and become smaller than the vibration signals of amide-I which gradually increase. This demonstrates the resonant nature of the plasmonic IRAS enhancement effect and shows the importance of the match between the plasmonic resonance and IR absorption modes which can achieve the maximum enhanced IR absorption signals. Moreover, enhancement factor (EF) is normally used to quantify the sensitivity of plasmonically-enhanced IRAS effect and it is described as [87, 90]:

$$EF = \frac{\Delta R}{\Delta R_0} \bullet \frac{A_0}{A_{SEIRA}} \tag{1}$$

where ΔR is calculated as the reflectance difference between the gold micro-flake array's IR spectra before and after baseline correction which is equal to 9%, ΔR_0 is calculated as the reflectance difference between flat unstructured gold mirror without BSA coating and flat unstructured gold mirror coated with BSA of the same concentration which turns out to be around 0.1%. In terms of the A_0 and A_{SEIRA}, the former one is the whole area containing gold micro-flakes arrays exposed to the incident light which is 240 × 240 μm^2, and A_{SEIRA} is the entire gold micro-flakes surfaces corresponding to ~ 7350 μm^2. Therefore, we obtained an enhancement factor of ~ 705. This factor is relatively smaller than the reported values of nanometer-sized antennasand it can be explained by the low aspect ratio of our gold micro-flakes resulting in less confined electromagnetic near fields.

In order to investigate the detection limit of our plasmonic substrates, the gold micro-flakes arrays with 2.1 μm L and 3.9 μm P were utilized as sensing substrates which have plasmonic resonance wavelength located at around 1660 cm^{-1} resulting in a perfect

match between it and amide I band. Their responses to BSA at several concentrations are presented in **Fig. 4.6**. The detection limit of 10 nM was obtained and their responses followed a nonlinear increase in the amide I band intensity.
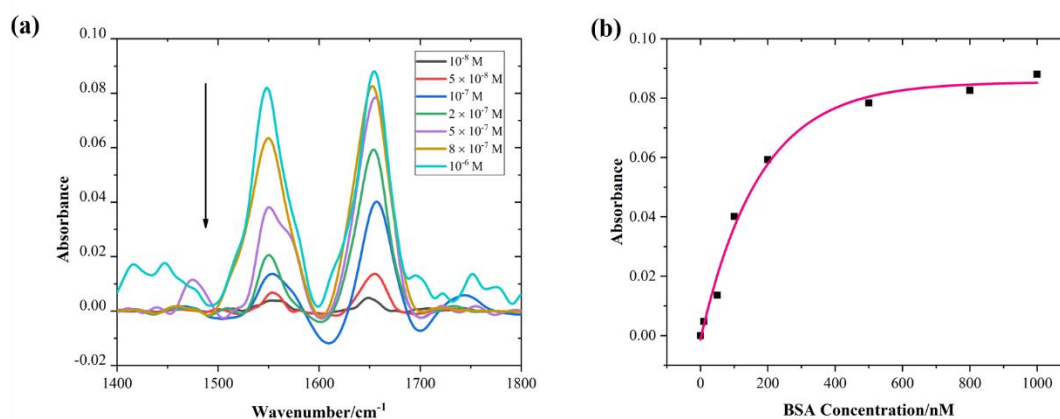
Figure 4.6 (a) Spectra of gold micro-flakes + BSA with different concentrations after baseline correction. (b) The intensity of the amide I band (black square) calculated from the spectra in (a) versus BSA concentration. The red line is the fitting curve. The gold micro-flakes arrays with the length of 2.1 μm and the period of 3.9 μm were used as the sensing substrate.

4. 5 Summary

The precision photoreduction technology described in **Chapter 2** has been applied to fabricate plasmonic structures of gold micro-flake arrays, whose plasmonic resonances in the IR range can be precisely tuned through the control of fabrication parameters. The IR reflectance spectra of the plasmonic structures with different geometric paramters have been measured using an IR microscope. The experimental results have been compared and matched well with numerical simulation results. Moreover, the fabricated arrays of gold micro-flakes has been experimentally demonstrated as a biochemical sensor to detect standard protein-bovine serum albumin (BSA). An enhancement factor of ~705 was obtained, and the limit of detection for

BSA was at the concentration level of 10 nM. In experiments, the precision photoreduction technology has showed its great flexibility on rapid printing of plasmonic structures, which provides an attractive cost-effective solution for fabricating plasmonic nanophotonic devices and sensors.

Chapter 5
Summary and Outlook

5. 1 Summary

In this thesis, with a precision photoreduction technology, two kinds of LSPR-based plasmonic structures are designed and fabricated on multi-mode fiber end-faces and silica wafers, respectivley. This technology can overcome the drawbacks of conventional micro/nano fabrication techniques, which are typically expensive and time-consuming, and enable a direct and rapid fabrication of plasmonic structures in a cost-effective way and thereby may unlock the full potential of plasmonic devices. One of the merits of the precision photoreduction technology is that the growth of metal nanoparticles can be precisely controlled by the utilized DMD-based optical exposure system through exposure doses and designed patterns. However, the resolution of this fabrication technology can be further improved towards nanofabrication.

For the first kind of plasmonic biosensors, micropatterns of gold nanoparticles are directly printed on the end-face of a multi-mode optical fiber. The AuNPs are thermally treated to improve the surface smoothness and degree of crystallinity. The spectral responses of the printed AuNPs with different sizes have been characterized and utilized for label-free biosensing. Such an ultraminiature fiber-tip printed-plasmonic biosensor offers a cost-effective biodetection technology for a myriad of applications ranging from point-of-care testing to in vivo diagnosis of stubborn diseases.

Moreover, plasmonic arrays of gold micro-flakes have been designed and fabricated on the silica wafer. The IR response of the sensor is analyzed by the FEM method and a good agreement with experimental results has been achieved. A plasmonically-enhanced IRAS biochemical sensing using the arrays of gold micro-flakes has been experimentally demonstrated to detect BSA protein.

5. 2 Future works

These two works presented in this thesis have demonstrated the great potential of the plasmonic structures fabricated by precision photoreduction technology. However, both of micropatterns of AuNPs and gold micro-flakes are in micrometer scale. The performance of optical fiber-tip plasmonic biosensors can be further improved if precisely arrayed gold nanoparticles can be fabricated on the fiber end surface by using e.g. a template-assisted precision photoreduction technology. Gold nanorods or nanobipyramids with improved uniformity may further improve the sensitivity of the sensor through the enhancement of surface plasmon resonance and its interaction with biomolecules. Moreover, a single-mode optical fiber working at the wavelength of 633 nm may also be used to improve the transmission stability of spectral signals and thus is conducive to lower detection limit.

In the second work, the geometry of each element in periodic plasmonic structures can be further improved through a more systematic optimization on fabrication processes. Then, the width of gold micro-flakes can be reduced to increase their aspect

ratio. A larger aspect ratio can provide a higher electric field enhancement and thereby may improve the performance of such a structure on plasmonically-enhanced IRAS biosensing. Moreover, the geometry of plasmonic SLR structures can be further devised to introduce e.g. Fano resonance or bound state in the continuum, towards the development of plasmonic metasurface or metamaterial biosensor. For example, an asymmetric metamaterial with two coupled modes enrich the spectral resonances for multi-parameter biochemical sensing.

References

1. Kelly, K. L., Coronado, E., Zhao, L. L., & Schatz, G. C. (2003). The optical properties of metal nanoparticles: the influence of size, shape, and dielectric environment. *The Journal of Physical Chemistry B*, *107*(3), 668-677.

2. Schlücker, S. (2014). Surface-Enhanced raman spectroscopy: Concepts and chemical applications. *Angewandte Chemie International Edition*, *53*(19), 4756-4795.

3. Bauch, M., Toma, K., Toma, M., Zhang, Q., & Dostalek, J. (2014). Plasmon-enhanced fluorescence biosensors: a review. *Plasmonics*, *9*(4), 781-799.

4. Neubrech, F., Huck, C., Weber, K., Pucci, A., & Giessen, H. (2017). Surface-enhanced infrared spectroscopy using resonant nanoantennas. *Chemical Reviews*, *117*(7), 5110-5145.

5. Pines, D. (1956). Collective energy losses in solids. *Reviews of modern physics*, *28*(3), 184.

6. Ritchie, R. H. (1957). Plasma losses by fast electrons in thin films. *Physical review*, *106*(5), 874.

7. Willets, K. A., & Van Duyne, R. P. (2007). Localized surface plasmon resonance spectroscopy and sensing. *Annual review of physical chemistry*, *58*(1), 267-297.

8. Mayer, K. M., & Hafner, J. H. (2011). Localized surface plasmon resonance sensors. *Chemical Reviews*, *111*(6), 3828-3857.

9. Maier, S. A. (2007). *Plasmonics: fundamentals and applications* (Vol. 1, p. 245). New York: springer.

10. West, P. R., Ishii, S., Naik, G. V., Emani, N. K., Shalaev, V. M., & Boltasseva, A. (2010). Searching for better plasmonic materials. *Laser & photonics reviews*, *4*(6), 795-808.

11. Gwon, H. R., & Lee, S. H. (2010). Spectral and angular responses of surface plasmon resonance based on the Kretschmann prism configuration. *Materials transactions*, *51*(6), 1150-1155.

12. Su, W. (2017). Design of high performance surface plasmon resonance biosensor

using silver-based sinusoidal diffraction grating. *Optik*, *131*, 104-109.

13. Urrutia, A., Bojan, K., Marques, L., Mullaney, K., Goicoechea, J., James, S., Matt, C., Tatam, R. & Korposh, S. (2016). Novel highly sensitive protein sensors based on tapered optical fibres modified with Au-based nanocoatings. *Journal of Sensors*, *2016*.

14. Gordon Ii, J. G., & Ernst, S. (1980). Surface plasmons as a probe of the electrochemical interface. *Surface Science*, *101*(1-3), 499-506.

15. Liedberg, B., Nylander, C., & Lunström, I. (1983). Surface plasmon resonance for gas detection and biosensing. *Sensors and actuators*, *4*, 299-304.

16. Liedberg, B., Nylander, C., & Lundström, I. (1995). Biosensing with surface plasmon resonance—how it all started. *Biosensors and Bioelectronics*, *10*(8), i-ix.

17. Haes, A. J., & Van Duyne, R. P. (2002). A nanoscale optical biosensor: sensitivity and selectivity of an approach based on the localized surface plasmon resonance spectroscopy of triangular silver nanoparticles. *Journal of the American Chemical Society*, *124*(35), 10596-10604.

18. Anker, J. N., Hall, W. P., Lyandres, O., Shah, N. C., Zhao, J., & Van Duyne, R. P. (2008). Biosensing with plasmonic nanosensors. *Nature materials*, *7*(6), 442-453.

19. Chen, H., Kou, X., Yang, Z., Ni, W., & Wang, J. (2008). Shape-and size-dependent refractive index sensitivity of gold nanoparticles. *Langmuir*, *24*(10), 5233-5237.

20. Sherry, L. J., Chang, S. H., Schatz, G. C., Van Duyne, R. P., Wiley, B. J., & Xia, Y. (2005). Localized surface plasmon resonance spectroscopy of single silver nanocubes. *Nano letters*, *5*(10), 2034-2038.

21. Shen, Y., Zhou, J., Liu, T., Tao, Y., Jiang, R., Liu, M., Xiao, G., Zhu, J., Zhou, Z., Wang, X., Jin, C. & Wang, J. (2013). Plasmonic gold mushroom arrays with refractive index sensing figures of merit approaching the theoretical limit. *Nature communications*, *4*(1), 1-9.

22. Phillips, K. S. (2008). Jirí Homola (Ed.): Surface plasmon resonance-based sensors.

23. Tetz, K. A., Pang, L., & Fainman, Y. (2006). High-resolution surface plasmon resonance sensor based on linewidth-optimized nanohole array

transmittance. *Optics letters*, *31*(10), 1528-1530.

24. Riboh, J. C., Haes, A. J., McFarland, A. D., Ranjit Yonzon, C., & Van Duyne, R. P. (2003). A nanoscale optical biosensor: real-time immunoassay in physiological buffer enabled by improved nanoparticle adhesion. *The Journal of Physical Chemistry B*, *107*(8), 1772-1780.

25. Yonzon, C. R., Jeoung, E., Zou, S., Schatz, G. C., Mrksich, M., & Van Duyne, R. P. (2004). A comparative analysis of localized and propagating surface plasmon resonance sensors: the binding of concanavalin A to a monosaccharide functionalized self-assembled monolayer. *Journal of the American Chemical Society*, *126*(39), 12669-12676.

26. Gong, Y., Chang, L., Viola, K. L., Lacor, P. N., Lambert, M. P., Finch, C. E., Krafft, G. A., & Klein, W. L. (2003). Alzheimer's disease-affected brain: presence of oligomeric Aβ ligands (ADDLs) suggests a molecular basis for reversible memory loss. *Proceedings of the National Academy of Sciences*, *100*(18), 10417-10422.

27. Lambert, M. P., Barlow, A. K., Chromy, B. A., Edwards, C., Freed, R., Liosatos, M., Morgan, T. E., Rozovsky, I., Trommer, B., Viola, K. L., Wals, P., Zhang, C., Finch,C. E., Krafft, G. A. & Klein, W. L. (1998). Diffusible, nonfibrillar ligands derived from Aβ1–42 are potent central nervous system neurotoxins. *Proceedings of the National Academy of Sciences*, *95*(11), 6448-6453.

28. Lambert, M. P., Viola, K. L., Chromy, B. A., Chang, L., Morgan, T. E., Yu, J., Venton, D. L., Krafft, G. A., Finch, C. E. & Klein, W. L. (2001). Vaccination with soluble Aβ oligomers generates toxicity-neutralizing antibodies. *Journal of neurochemistry*, *79*(3), 595-605.

29. Haes, A. J., Chang, L., Klein, W. L., & Van Duyne, R. P. (2005). Detection of a biomarker for Alzheimer's disease from synthetic and clinical samples using a nanoscale optical biosensor. *Journal of the American Chemical Society*, *127*(7), 2264-2271.

30. Neubrech, F., Huck, C., Weber, K., Pucci, A., & Giessen, H. (2017). Surface-enhanced infrared spectroscopy using resonant nanoantennas. *Chemical*

Reviews, *117*(7), 5110-5145.

31. Kundu, J., Le, F., Nordlander, P., & Halas, N. J. (2008). Surface enhanced infrared absorption (SEIRA) spectroscopy on nanoshell aggregate substrates. *Chemical Physics Letters*, *452*(1-3), 115-119.

32. Adato, R., & Altug, H. (2013). In-situ ultra-sensitive infrared absorption spectroscopy of biomolecule interactions in real time with plasmonic nanoantennas. *Nature communications*, *4*(1), 1-10.

33. Neubrech, F., Pucci, A., Cornelius, T. W., Karim, S., García-Etxarri, A., & Aizpurua, J. (2008). Resonant plasmonic and vibrational coupling in a tailored nanoantenna for infrared detection. *Physical review letters*, *101*(15), 157403.

34. Hartstein, A., Kirtley, J. R., & Tsang, J. C. (1980). Enhancement of the infrared absorption from molecular monolayers with thin metal overlayers. *Physical Review Letters*, *45*(3), 201.

35. Adato, R., Yanik, A. A., Amsden, J. J., Kaplan, D. L., Omenetto, F. G., Hong, M. K., Erramilli, S. & Altug, H. (2009). Ultra-sensitive vibrational spectroscopy of protein monolayers with plasmonic nanoantenna arrays. *Proceedings of the National Academy of Sciences*, *106*(46), 19227-19232.

36. Bagheri, S., Weber, K., Gissibl, T., Weiss, T., Neubrech, F., & Giessen, H. (2015). Fabrication of square-centimeter plasmonic nanoantenna arrays by femtosecond direct laser writing lithography: effects of collective excitations on SEIRA enhancement. *ACS Photonics*, *2*(6), 779-786.

37. Wang, T., Nguyen, V. H., Buchenauer, A., Schnakenberg, U., & Taubner, T. (2013). Surface enhanced infrared spectroscopy with gold strip gratings. *Optics express*, *21*(7), 9005-9010.

38. Cohn, B., Das, K., Basu, A., & Chuntonov, L. (2021). Infrared open cavities for strong vibrational coupling. *The Journal of Physical Chemistry Letters*, *12*(29), 7060-7066.

39. Abb, M., Wang, Y., Papasimakis, N., De Groot, C. H., & Muskens, O. L. (2014). Surface-enhanced infrared spectroscopy using metal oxide plasmonic antenna

arrays. *Nano letters*, *14*(1), 346-352.

40. Chen, K., Duy Dao, T., & Nagao, T. (2017). Tunable nanoantennas for surface enhanced infrared absorption spectroscopy by colloidal lithography and post-fabrication etching. *Scientific reports*, *7*(1), 1-8.

41. Brown, L. V., Yang, X., Zhao, K., Zheng, B. Y., Nordlander, P., & Halas, N. J. (2015). Fan-shaped gold nanoantennas above reflective substrates for surface-enhanced infrared absorption (SEIRA). *Nano letters*, *15*(2), 1272-1280.

42. Lin, Y., Zou, Y., & Lindquist, R. G. (2011). A reflection-based localized surface plasmon resonance fiber-optic probe for biochemical sensing. *Biomedical optics express*, *2*(3), 478-484.

43. Pető, G., Molnar, G. L., Paszti, Z., Geszti, O., Beck, A., & Guczi, L. (2002). Electronic structure of gold nanoparticles deposited on SiOx/Si (100). *Materials Science and Engineering: C*, *19*(1-2), 95-99.

44. Schaub, A., Slepička, P., Kašpárková, I., Malinský, P., Macková, A., & Švorčík, V. (2013). Gold nanolayer and nanocluster coatings induced by heat treatment and evaporation technique. *Nanoscale research letters*, *8*(1), 1-8.

45. Hezard, T., Fajerwerg, K., Evrard, D., Collière, V., Behra, P., & Gros, P. (2012). Gold nanoparticles electrodeposited on glassy carbon using cyclic voltammetry: Application to Hg (II) trace analysis. *Journal of Electroanalytical Chemistry*, *664*, 46-52.

46. Liedberg, B., Nylander, C., & Lundström, I. (1995). Biosensing with surface plasmon resonance—how it all started. *Biosensors and Bioelectronics*, *10*(8), i-ix.

47. Lee, K. L., Wu, S. H., Lee, C. W., & Wei, P. K. (2011). Sensitive biosensors using Fano resonance in single gold nanoslit with periodic grooves. *Optics Express*, *19*(24), 24530-24539.

48. Lesuffleur, A., Im, H., Lindquist, N. C., & Oh, S. H. (2007). Periodic nanohole arrays with shape-enhanced plasmon resonance as real-time biosensors. *Applied Physics Letters*, *90*(24), 243110.

49. Xue, J., Zhou, W. Z., Dong, B. Q., Wang, X., Chen, Y., Huq, E., Zeng, W., Qu, X.

& Liu, R. (2009). Surface plasmon enhanced transmission through planar gold quasicrystals fabricated by focused ion beam technique. *Microelectronic engineering*, *86*(4-6), 1131-1133.

50. Skrabalak, S. E., Chen, J., Sun, Y., Lu, X., Au, L., Cobley, C. M., & Xia, Y. (2008). Gold nanocages: synthesis, properties, and applications. *Accounts of chemical research*, *41*(12), 1587-1595.

51. Henzie, J., Lee, M. H., & Odom, T. W. (2007). Multiscale patterning of plasmonic metamaterials. *Nature nanotechnology*, *2*(9), 549-554.

52. Wang, S., Sun, X., Ding, M., Peng, G., Qi, Y., Wang, Y., & Ren, J. (2018). The investigation of an LSPR refractive index sensor based on periodic gold nanorings array. *Journal of Physics D: Applied Physics*, *51*(4), 045101.

53. Bin-Alam, M. S., Reshef, O., Mamchur, Y., Alam, M. Z., Carlow, G., Upham, J., Sullivan, B. T., Menard, J., Huttunen, M. J., Boyd, R. W., & Dolgaleva, K. (2021). Ultra-high-Q resonances in plasmonic metasurfaces. *Nature communications*, *12*(1), 1-8.

54. Ni, X., Emani, N. K., Kildishev, A. V., Boltasseva, A., & Shalaev, V. M. (2012). Broadband light bending with plasmonic nanoantennas. *Science*, *335*(6067), 427-427.

55. Avayu, O., Almeida, E., Prior, Y., & Ellenbogen, T. (2017). Composite functional metasurfaces for multispectral achromatic optics. *Nature communications*, *8*(1), 1-7.

56. Chen, X., Huang, L., Mühlenbernd, H., Li, G., Bai, B., Tan, Q., Jin, G., Qiu, C., Zhang, S. & Zentgraf, T. (2012). Dual-polarity plasmonic metalens for visible light. *Nature communications*, *3*(1), 1-6.

57. Huang, L., Chen, X., Mühlenbernd, H., Zhang, H., Chen, S., Bai, B., Tan, Q., Jin, G., Cheah, K., Qiu, C., Li, J., Zentgraf, T., & Zhang, S. (2013). Three-dimensional optical holography using a plasmonic metasurface. *Nature communications*, *4*(1), 1-8.

58. Huang, L., Mühlenbernd, H., Li, X., Song, X., Bai, B., Wang, Y., & Zentgraf, T.

(2015). Broadband hybrid holographic multiplexing with geometric metasurfaces. *Advanced Materials*, *27*(41), 6444-6449.

59. Luo, X., Hu, Y., Li, X., Jiang, Y., Wang, Y., Dai, P., Liu, Q., Shu, Z., & Duan, H. (2020). Integrated metasurfaces with microprints and helicity-multiplexed holograms for real-time optical encryption. *Advanced Optical Materials*, *8*(8), 1902020.

60. Li, X., Chen, L., Li, Y., Zhang, X., Pu, M., Zhao, Z., Ma, X., Wang, Y., Hong, M., & Luo, X. (2016). Multicolor 3D meta-holography by broadband plasmonic modulation. *Science advances*, *2*(11), e1601102.

61. Yu, P., Li, J., Li, X., Schütz, G., Hirscher, M., Zhang, S., & Liu, N. (2019). Generation of switchable singular beams with dynamic metasurfaces. *ACS nano*, *13*(6), 7100-7106.

62. Li, J., Kamin, S., Zheng, G., Neubrech, F., Zhang, S., & Liu, N. (2018). Addressable metasurfaces for dynamic holography and optical information encryption. *Science advances*, *4*(6), eaar6768.

63. Yu, P., Li, J., Zhang, S., Jin, Z., Schütz, G., Qiu, C. W., Hirscher, M., & Liu, N. (2018). Dynamic Janus metasurfaces in the visible spectral region. *Nano letters*, *18*(7), 4584-4589.

64. Gierak, J., Madouri, A., Biance, A. L., Bourhis, E., Patriarche, G., Ulysse, C., Lucot, D., Lafosse, X., Auvray, L., Bruchhaus, L., & Jede, R. (2007). Sub-5 nm FIB direct patterning of nanodevices. *Microelectronic engineering*, *84*(5-8), 779-783.

65. Meng, F., Luo, G., Maximov, I., Montelius, L., Chu, J., & Xu, H. (2011). Fabrication and characterization of bilayer metal wire-grid polarizer using nanoimprint lithography on flexible plastic substrate. *Microelectronic engineering, 88*(10), 3108-3112.

66. Jacot-Descombes, L., Cadarso, V. J., Schleunitz, A., Grützner, S., Klein, J. J., Brugger, J., Schift, H. & Grützner, G. (2015). Organic-inorganic-hybrid-polymer microlens arrays with tailored optical characteristics and multi-focal properties. *Optics Express, 23*(19), 25365-25376.

67. Zheng, L., Zywietz, U., Evlyukhin, A., Roth, B., Overmeyer, L., & Reinhardt, C. (2019). Experimental demonstration of surface plasmon polaritons reflection and transmission effects. *Sensors, 19*(21), 4633.

68. Kumar, K., Duan, H., Hegde, R. S., Koh, S. C., Wei, J. N., & Yang, J. K. (2012). Printing colour at the optical diffraction limit. *Nature nanotechnology*, *7*(9), 557-561.

69. Zhang, Y., Zhang, Q., Ouyang, X., Lei, D. Y., Zhang, A. P., & Tam, H. Y. (2018). Ultrafast light-controlled growth of silver nanoparticles for direct plasmonic color printing. *ACS nano*, *12*(10), 9913-9921.

70. Zhang, Y., Liang, Z., Zhang, A. P., & Tam, H. Y. (2021). Direct Printing of Micropatterned Plasmonic Substrates of Size-Controlled Gold Nanoparticles by Precision Photoreduction. *Advanced Optical Materials*, *9*(1), 2001368.

71. Willets, K. A., & Van Duyne, R. P. (2007). Localized surface plasmon resonance spectroscopy and sensing. *Annual review of physical chemistry*, *58*(1), 267-297.

72. Liz-Marzán, L. M. (2006). Tailoring surface plasmons through the morphology and assembly of metal nanoparticles. *Langmuir*, *22*(1), 32-41.

73. Lu, X., Rycenga, M., Skrabalak, S. E., Wiley, B., & Xia, Y. (2009). Chemical synthesis of novel plasmonic nanoparticles. *Annual review of physical chemistry*, *60*, 167-192.

74. Ricciardi, A., Crescitelli, A., Vaiano, P., Quero, G., Consales, M., Pisco, M., Esposito, E., & Cusano, A. (2015). Lab-on-fiber technology: a new vision for chemical and biological sensing. *Analyst*, *140*(24), 8068-8079.

75. Caucheteur, C., Guo, T., & Albert, J. (2015). Review of plasmonic fiber optic biochemical sensors: improving the limit of detection. *Analytical and bioanalytical chemistry*, *407*(14), 3883-3897.

76. Wang, X. D., & Wolfbeis, O. S. (2016). Fiber-optic chemical sensors and biosensors (2013–2015). *Analytical chemistry*, *88*(1), 203-227.

77. Xiang, D., Zhai, K., Xiang, W., & Wang, L. (2014). Highly sensitive fluorescence quantitative detection of specific DNA sequences with molecular beacons and

nucleic acid dye SYBR Green I. *Talanta*, *129*, 249-253.

78. Peng, Y., Huang, Y., Zhu, Y., Chen, B., Wang, L., Lai, Z., Zhang, Z., Zhao, M., Tan, C., Yang, N., Shao, F., Han, Y., & Zhang, H. (2017). Ultrathin two-dimensional covalent organic framework nanosheets: preparation and application in highly sensitive and selective DNA detection. *Journal of the American Chemical Society*, *139*(25), 8698-8704.

79. Smith, B. C. (2011). *Fundamentals of Fourier transform infrared spectroscopy*. CRC press.

80. Hoang, C. V., Oyama, M., Saito, O., Aono, M., & Nagao, T. (2013). Monitoring the presence of ionic mercury in environmental water by plasmon-enhanced infrared spectroscopy. *Scientific reports*, *3*(1), 1-6.

81. Perry, D. A., Borchers, R. L., Golden, J. W., Owen, A. R., Price, A. S., Henry, W. A., Watanabe, F., & Biris, A. S. (2013). Surface-enhanced infrared absorption on elongated nickel nanostructures. *The Journal of Physical Chemistry Letters*, *4*(22), 3945-3949.

82. Cataldo, S., Zhao, J., Neubrech, F., Frank, B., Zhang, C., Braun, P. V., & Giessen, H. (2012). Hole-mask colloidal nanolithography for large-area low-cost metamaterials and antenna-assisted surface-enhanced infrared absorption substrates. *ACS nano*, *6*(1), 979-985.

83. Frank, B., Yin, X., Schäferling, M., Zhao, J., Hein, S. M., Braun, P. V., & Giessen, H. (2013). Large-area 3D chiral plasmonic structures. *ACS nano*, *7*(7), 6321-6329.

84. Aksu, S., Cetin, A. E., Adato, R., & Altug, H. (2013). Plasmonically enhanced vibrational biospectroscopy using low-cost infrared antenna arrays by nanostencil lithography. *Advanced Optical Materials*, *1*(11), 798-803.

85. Aksu, S., Yanik, A. A., Adato, R., Artar, A., Huang, M., & Altug, H. (2010). High-throughput nanofabrication of infrared plasmonic nanoantenna arrays for vibrational nanospectroscopy. *Nano letters*, *10*(7), 2511-2518.

86. Auzelyte, V., Gallinet, B., Flauraud, V., Santschi, C., Dutta-Gupta, S., Martin, O. J., & Brugger, J. (2013). Large-area gold/parylene plasmonic nanostructures

fabricated by direct nanocutting. *Advanced Optical Materials*, *1*(1), 50-54.

87. Neubrech, F., Huck, C., Weber, K., Pucci, A., & Giessen, H. (2017). Surface-enhanced infrared spectroscopy using resonant nanoantennas. *Chemical Reviews*, *117*(7), 5110-5145.

88. Braun, A., & Maier, S. A. (2016). Versatile direct laser writing lithography technique for surface enhanced infrared spectroscopy sensors. *ACS Sensors*, *1*(9), 1155-1162.

89. Weber, D., Albella, P., Alonso-González, P., Neubrech, F., Gui, H., Nagao, T., Hillenbrand, R., Aizpurua, J., & Pucci, A. (2011). Longitudinal and transverse coupling in infrared gold nanoantenna arrays: long range versus short range interaction regimes. *Optics express*, *19*(16), 15047-15061.

90. Di Meo, V., Caporale, A., Crescitelli, A., Janneh, M., Palange, E., De Marcellis, A., Portaccio, M., Lepore, M., Rendina, I., Ruvo, M., & Esposito, E. (2019). Metasurface based on cross-shaped plasmonic nanoantennas as chemical sensor for surface-enhanced infrared absorption spectroscopy. *Sensors and Actuators B: Chemical*, *286*, 600-607.